

Morten Elias Lødemel and Bertine Nergård

# Fiber Bragg Grating Optical Sensors for Strain and Temperature Monitoring of Lithium-Ion Coin Cells

Master's thesis in Energy and Environmental Engineering

Supervisor: Steven T. Boles

June 2024



Morten Elias Lødemel and Bertine Nergård

# **Fiber Bragg Grating Optical Sensors for Strain and Temperature Monitoring of Lithium-Ion Coin Cells**

Master's thesis in Energy and Environmental Engineering  
Supervisor: Steven T. Boles  
June 2024

Norwegian University of Science and Technology  
Faculty of Engineering  
Department of Energy and Process Engineering





---

## Preface


This thesis is submitted as the final work in the Master's Degree Program Energy and Environmental Engineering at the Norwegian University of Science and Technology (NTNU), Faculty of Engineering, Department of Energy and Process Engineering. This thesis fulfills the requirement for the award of the Master of Science degree and carries a credit value of 30 ECTs. The project focuses on advanced topics within energy and environmental engineering, incorporating practical experimentation and theoretical analysis to propose innovative solutions.

Throughout this thesis, the principles of coin cell assembly and the utilization of fiber Bragg grating optical fibers are explored. This work represents a continuation of a previous project assignment, underscoring its developmental and academic progression within the prescribed curriculum.

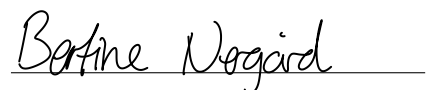
The authors would like to thank our supervisor, Steven Boles, for support and intellectual insight during the process of the project, as well as Markus Wahl for guidance with FBGs and Xiaoyang Guo for helping us with coin cell assembly, data interpretation, and more. Further, we would like to express our gratitude towards the Norwegian University of Science and Technology, the Faculty of Engineering, and the Department of Energy and Process Engineering for facilitating a workplace, instruments, and materials for this project work. Lastly, we would like to thank our co-students for their camaraderie and collaborative spirit throughout our studies. The supportive and engaging environment they helped create was not only instrumental in overcoming the many challenges we faced but also enriched our learning experience, making our journey both enjoyable and memorable. Their insights and encouragement have been invaluable, fostering a sense of community and friendship that we will cherish beyond our time at NTNU.

Date: June 5, 2024

Place: Trondheim, Norway



Morten Elias Lødemel



Bertine Nergård

## Abstract

This thesis investigates the application of fiber Bragg grating (FBG) optical sensors for real-time monitoring of lithium-ion coin cells, with a focus on their potential to enhance battery safety and longevity through precise monitoring of strain and temperature. The study utilized lab-made lithium-ion coin cells composed of lithium nickel manganese cobalt oxide (NMC111) as the cathode and artificial graphite (AG) as the anode.

The experimental work involved the assembly of coin cells and incorporating FBGs on the surface of the cells to perform measurements during cycling. The FBGs monitored external mechanical and thermal changes during different battery cycling conditions such as battery formation, cycling, aging, and under abusive conditions. One of the main limitations of dual-parameter monitoring is the necessity of a good method for decoupling the parameters, as well as minimizing background noise. Through the reference sensor method, the setup chosen allowed for dual-parameter monitoring, providing valuable insights into the battery's operational state.

FBG sensors have proven to be an effective tool for enhancing safety and performance in lithium-ion batteries by providing real-time strain and temperature measurements. Direct correlations between strain and SoC or SoH were not observed due to the small variations and hard casing of the coin cells. However, significant findings from the study demonstrated that FBGs could detect deformations and temperature changes, providing useful real-time monitoring for battery management systems. This capability showed good results for early prediction of failure through detecting a rapid increase in strain. Volume expansion indicates substantial gas formation, an early indicator of thermal runaway. In this setup, strain measurements were found to be a more reliable indicator of battery malfunction than temperature measurements.

## Sammendrag

Denne masteroppgaven tar for seg bruk av fiber optiske sensorer, nærmere bestemt Fiber Bragg Grating (FBG) sensorer, til å utføre målinger på litiumionbatterier i form av knappeceller. FBG sensorer har som egenskap å måle temperatur og deformasjon i sanntid. Hypotesen oppgaven bygger seg på er at ved å måle disse parameterene, kan man øke sikkerheten og levetiden til batterier. Studien baserer seg på knappeceller bestående av grafitt (AG) anode og litium nikkell mangan kobolt (NMC111) katode.

Labarbeidet innebar sammensetting av knappeceller, montering av FBG på overflaten, for så å måle temperatur og deformasjon under forskjellige opp- og utlandings sykluser. Dette innebar både formasjons sykluser, normale opp- og utlandinger, og under ekstreme forhold. Dette gav verdifulle resultater om batterienes tilstand. Ettersom FBG måler to parameter om gangen, var en av utfordringene i oppgaven å adskille endringene i den reflekterte bølgelengden til henholdsvis temperatur og deformasjon.

Under dette og andres arbeid har FBG vist seg som effektive sensorer til å bedre sikkerhet og ytelse til litiumionbatterier. Tidligere studier har funnet gode korrelasjoner mellom den reflekterte bølgelengden og de to batteriparameterne SoC (ladningsstatus) og SoH (helsestatus). Dette ble ikke observert under dette studiet, trolig grunnet en kombinasjon av det harde skallet til knappeceller, små variasjoner i temperatur og ekspansjon under normal bruk, samt for høy bakgrunnstøy som påvirket den reflekterte bølgelengden. Det som derimot ble observert er at FBG kan bli brukt til tidlig oppdaging av feil i batterier, ettersom FBG kan måle ekspansjon. Ekspansjon kan komme som følge av gassutvikling i batteriene, som kan resultere i en selvforsterkende overopphetnings reaksjon (thermal runaway), som i verstfall kan føre til brann og eksplosjoner. Målingene viste også god korrelasjon mellom batterifeil og temperaturøkning, men det ble konkludert med at deformasjonsmålingne var mer pålitlige til å indikere feil i batterier.

---

# Table of Contents

|  |             |
|--|-------------|
| <b>Preface</b>   | <b>i</b>    |
| <b>Abstract</b>  | <b>ii</b>   |
| <b>Sammendrag</b>  | <b>iii</b>  |
| <b>List of Figures</b>   | <b>vii</b>  |
| <b>List of Tables</b>  | <b>viii</b> |
| <b>List of Abbreviations</b>                                       | <b>ix</b>   |
| <b>1 Introduction</b>  | <b>1</b>    |
| 1.1 Objective . . . . .  | 2           |
| 1.2 Project Background . . . . .                                   | 2           |
| <b>2 Theory</b>  | <b>4</b>    |
| 2.1 Lithium-Ion Batteries . . . . .                                | 4           |
| 2.2 Anode and Cathode Materials in Lithium-Ion Batteries . . . . . | 8           |
| 2.2.1 Anode Materials . . . . .                                    | 9           |
| 2.2.2 Cathode Materials . . . . .                                  | 10          |
| 2.2.3 Electrolyte . . . . .  | 11          |
| 2.2.4 Separator . . . . .  | 11          |
| 2.2.5 Current Collector . . . . .                                  | 11          |
| 2.3 Battery State Parameters . . . . .                             | 12          |
| 2.3.1 State of Charge . . . . .                                    | 12          |
| 2.3.2 State of Health . . . . .                                    | 13          |
| 2.3.3 C-rate . . . . .   | 13          |
| 2.4 Battery Manufacturing . . . . .                                | 14          |
| 2.4.1 Battery Assembly . . . . .                                   | 14          |
| 2.4.2 Formation . . . . .  | 16          |
| 2.4.3 Contamination . . . . .                                      | 16          |
| 2.5 Battery Degradation . . . . .                                  | 17          |
| 2.5.1 SEI Layer Formation and Lithium Plating . . . . .            | 18          |
| 2.5.2 Surface Polarization and Structural Changes . . . . .        | 19          |
| 2.5.3 Thermal Runaway . . . . .                                    | 19          |
| 2.5.4 Gas Formation . . . . .                                      | 20          |
| 2.6 Sensing in Batteries . . . . .                                 | 21          |
| 2.6.1 Thermal Sensing Techniques for LIBs . . . . .                | 21          |
| 2.6.2 Volume Expansion Sensing Techniques for LIBs . . . . .       | 22          |
| 2.6.3 Optical Fiber Sensors . . . . .                              | 23          |
| 2.6.4 Fiber Bragg Grating Sensors . . . . .                        | 24          |
| 2.6.5 External Temperature Monitoring . . . . .                    | 26          |



---

|   |   |            |
|---|---|------------|
| 2.6.6   | Strain Monitoring . . . . .   | 26         |
| 2.6.7   | Dual-Parameter Measurements . . . . .   | 27         |
| <b>3</b>  | <b>Method</b>   | <b>29</b>  |
| 3.1   | Materials and Equipment . . . . .   | 29         |
| 3.1.1   | Electrodes . . . . .  | 29         |
| 3.1.2   | Electrolyte . . . . .   | 30         |
| 3.1.3   | Separators . . . . .  | 30         |
| 3.1.4   | FBG Sensors . . . . .   | 30         |
| 3.2   | Coin Cell Assembly . . . . .  | 30         |
| 3.2.1   | Material Preparation and Assembly . . . . .   | 30         |
| 3.2.2   | Challenges, Adjustments and Sources of Error . . . . .                                    | 31         |
| 3.3   | Formation Cycle . . . . .   | 31         |
| 3.4   | Coin Cell Cycling . . . . .   | 32         |
| 3.5   | FBG Calibration . . . . .   | 32         |
| 3.5.1   | Calibration Results . . . . .   | 33         |
| 3.6   | Coin Cell Setup With FBGs . . . . .   | 34         |
| 3.7   | Data Analysis . . . . .   | 36         |
| <b>4</b>  | <b>Results and Discussion</b>   | <b>37</b>  |
| 4.1   | Formation Cycles . . . . .  | 37         |
| 4.2   | Correlation Between Strain and Battery Degradation Through Long-Term<br>Cycling . . . . . | 40         |
| 4.3   | Correlation Between FBG Measurements and Battery Malfunctioning . . . . .                 | 42         |
| 4.3.1   | Using FBGs to Detect Battery Malfunctioning . . . . .                                     | 42         |
| 4.3.2   | Formation Cycles . . . . .  | 46         |
| 4.4   | Detecting Battery Malfunctioning Under Abusive Conditions . . . . .                       | 52         |
| 4.4.1   | Coin Cell X . . . . .   | 52         |
| 4.4.2   | Coin Cell Y . . . . .   | 53         |
| 4.4.3   | Coin Cell Z . . . . .   | 54         |
| 4.4.4   | Strain and Temperature Behaviour vs. Charge Transfer . . . . .                            | 55         |
| 4.5   | Relationship Between Strain and SoC . . . . .   | 55         |
| <b>5</b>  | <b>Conclusion</b>   | <b>57</b>  |
| <b>6</b>  | <b>Further Work</b>   | <b>58</b>  |
| <b>Appendix A Fiber Bragg Grating Calibration</b> |   | <b>A-1</b> |
| <b>Appendix B Battery Capacity</b>                |   | <b>B-1</b> |

## List of Figures

|      |   |    |
|------|---|----|
| 2.1  | a) Discharge and b) charge for a lithium-ion battery. [9] . . . . .   | 5  |
| 2.2  | Stages of intercalation and de-intercalation in a graphite anode. [19] . . . . .  | 6  |
| 2.3  | Cell polarization as a function of operating current. [20] . . . . .  | 8  |
| 2.4  | Chemical structure of lithium-ion battery. [24] . . . . .   | 9  |
| 2.5  | Structure of the three lithium-insertion compounds; layered, spinel, and olivine. [29] . . . . .  | 11 |
| 2.6  | Main steps of the battery assembly process (adapted from [38]). . . . .   | 14 |
| 2.7  | Different cell geometries, (a) cylindrical (b) coin (c) prismatic (d) pouch. [24] . . . . .   | 15 |
| 2.8  | SEI layer formation and lithium plating on graphite anode (adapted from [11]). . . . .  | 18 |
| 2.9  | Working principle of FBG. (a) An FBG with no effect from strain or heat; (b) Strain-affected FBG, changing the grating spacing, causing a shift in the Bragg wavelength; (c) Heat-affected FBG where the wavelength shifts as the effective refractive index of the gratings change. [73] . . . . . | 25 |
| 3.1  | Project method. . . . .   | 29 |
| 3.2  | Schematic of coin cell assembly. [84] . . . . .   | 31 |
| 3.3  | Results from FBG calibration. . . . .   | 34 |
| 3.4  | FBG setup for strain and temperature measurements on a coin cell. . . . .   | 35 |
| 4.1  | Formation cycles at C/10 for a NMC111/graphite coin cell with simultaneous strain measurements from FBGs. . . . .   | 37 |
| 4.2  | Formation cycles at C/10 for a NMC111/graphite coin cell with simultaneous strain measurements from FBGs. . . . .   | 38 |
| 4.3  | Battery cycled at C/3 for 449 cycles. . . . .   | 41 |
| 4.4  | Strain change during constant voltage at 4.2 V and the corresponding voltage and current signals for the malfunctioning battery. . . . .  | 42 |
| 4.5  | Strain change during constant voltage at 4.2 V and the corresponding voltage and current signals for the normal battery. . . . .  | 43 |
| 4.6  | Strain change vs. charge transfer for the normal and malfunctioning battery. . . . .  | 44 |
| 4.7  | Temperature change vs. charge transfer for the normal and malfunctioning battery. . . . .   | 44 |
| 4.8  | Voltage and current profile vs. time for the formation cycling of the malfunctioning coin cell. . . . .   | 47 |
| 4.9  | Charge and discharge capacity over the first five cycles during formation for the normal and malfunctioning coin cells. . . . .   | 48 |
| 4.10 | Differential capacity plot for the first charge cycle for the normal and malfunctioning coin cells. . . . .   | 49 |
| 4.11 | Differential capacity plot for the first discharge cycle for the normal and malfunctioning coin cells. . . . .  | 50 |
| 4.12 | Differential capacity plot for the second charge cycle for the normal and malfunctioning coin cells. . . . .  | 51 |

---

|      |  |     |
|------|--|-----|
| 4.13 | Strain and temperature signals during CV at 3 V, along with the corresponding voltage and current signals for coin cell X. . . . . | 52  |
| 4.14 | Strain and temperature signals during CV at 3 V, along with the corresponding voltage and current signals for coin cell Y. . . . . | 53  |
| 4.15 | Strain and temperature signals during CV at 3 V, along with the corresponding voltage and current signals for coin cell Z. . . . . | 54  |
| 4.16 | Strain change vs. charge transfer for the three coin cells. . . . .  | 55  |
| 4.17 | Temperature vs. charge transfer for the three coin cells. . . . .  | 55  |
| A.1  | Setup of the FBG calibration. . . . .  | A-1 |
| B.1  | Capacity for coin cell cycled at 0.33C, 0.44C and 0.55C, then back to 0.33C, for five cycles at each rate. . . . .                 | B-1 |

## List of Tables

|     |   |     |
|-----|---|-----|
| 1   | Overview of reused content from project assignment <i>Fiber Bragg Grating Optical Sensors for Strain and Temperature Sensing on Lithium-Ion Batteries</i> . . . . . | 3   |
| 2   | FBG calibration results. . . . .  | 33  |
| 3   | Mean charge and discharge capacity and corresponding efficiency and strain change during 4 cycles at C/3 after CVC for the coin cells. . . . .                      | 46  |
| A.1 | FBG specifications. . . . .   | A-1 |

## List of Abbreviations

| Abbreviation | Definition                            |
|--------------|---------------------------------------|
| AG           | Artificial Graphite                   |
| BMS          | Battery Management System             |
| CC           | Constant Current                      |
| C-rate       | Capacity-rate                         |
| CV           | Constant Voltage                      |
| CVC          | Constant Voltage Charge               |
| DoD          | Depth of Discharge                    |
| FBG          | Fiber Bragg Grating                   |
| SEI          | Solid Electrolyte Interphase          |
| LCO          | Lithium Cobalt Oxide                  |
| LFP          | Lithium Iron Phosphate                |
| LIB          | Lithium-Ion Battery                   |
| LMO          | Lithium Manganese Oxide               |
| NCA          | Lithium Nickel Cobalt Aluminium Oxide |
| NMC          | Lithium Nickel Manganese Cobalt Oxide |
| SoC          | State of Charge                       |
| SoH          | State of Health                       |

---

# 1 Introduction

Lithium-ion batteries (LIBs) have a wide range of applications, from small electric devices like computers and mobile phones to larger energy packs in vehicles and stationary backup systems [1]. Their high energy density and power density together with a low carbon footprint have evolved LIBs into a billion-dollar market [1, 2]. Additionally, the UN has proposed LIBs as one of the key contributors to reducing greenhouse gas emissions, especially in the transport and energy sectors. The transition towards a sustainable energy economy depends on the capacity to generate clean energy. However, clean energy from solar and wind power are weather-dependent, intermittent energy sources. Consequently, LIBs have emerged as a green and efficient energy storage solution capable of mitigating this issue. [3]

To ensure the further employment of LIBs it is crucial to continuously improve quality, reliability, longevity, and safety, while also focusing on price, volume, and weight reduction [4]. Addressing these challenges necessitates strengthening the current LIB design. Investigating new materials, structures, and sensing methods has been suggested as the way forward to tackle these obstacles.

One of the main hindrances to the full utilization of LIBs in the transport sector is the charge time. However, there are possibilities for improvement, especially in the automotive sector, where demands include high power, energy, and fast charging rates. Abusive cycling conditions, inherent in electric vehicle usage, lead to heat generation and non-uniform current distribution, making thermal management crucial for maintaining performance and ensuring safety. Elevated temperatures during fast charging contribute to accelerated battery degradation, underscoring the need for effective sensing mechanisms. [5]

Monitoring battery health during cycling is crucial, and the application of optical fiber sensing in LIBs has gained attention. Fiber Bragg gratings (FBGs), known for their high sensitivity to strain and temperature, have emerged as a valuable tool for real-time monitoring of LIBs. FBG sensing has the potential to enhance performance, extend battery lifetime, improve efficiency, and ensure safety. [4]

This master thesis utilizes FBGs for sensing lithium-ion coin cells. Using multiple fibers or multiplexed fibers with two or more gratings makes it possible to discriminate between temperature and strain contributions using the reference fiber method. This is done to isolate the strain caused by swelling during battery operation [6]. Battery swelling is mainly caused by either solid electrolyte interphase (SEI) formation or gas evolution within the battery cell. Gas evolution and SEI formation are normal behaviors for lithium-ion batteries and contribute to battery expansion mostly during the first cycles of a battery, better known as the formation cycles. During formation, the batteries undergo chemical activation, enabling such reactions. [7–9]

Extensive battery swelling can also occur as a result of battery malfunctioning. If a battery breaks down, unwanted side reactions may occur, leading to excessive gas production and

further expansion of the SEI layer. Such events can drastically reduce the efficiency and life expectancy of the battery, as well as pose significant safety risks due to the possibility of thermal runaway. In this context, the ability of FBGs to monitor strain and temperature simultaneously is critical. It allows for real-time, precise measurements that can detect early signs of battery failure. [10–12]

## 1.1 Objective

Most of the literature regarding the use of FBGs as temperature and strain sensors for LIBs focuses on pouch cells as they are widely used in the energy and transport sector. FBGs were first utilized for monitoring the external temperature on coin cells by Yang et. al [13] in 2013 and in 2017 by Fortier et. al [14] used embedded FBGs in coin cells. However, the authors of this thesis have not found any literature on measurements of external strain on coin cells using FBGs to estimate battery state parameters and correlating strain and temperature response with battery malfunctioning.

Hence, the primary objectives of this thesis are to: (1) assemble coin cells in the laboratory, and improve the assembly technique through the course of this work; (2) evaluate the impact of FBGs on the real-time monitoring capabilities of coin cells and; (3) assess the potential of this technology to predict and prevent failure of coin cells, mainly through external strain measurements and; (4) using the externally mounted FBGs to evaluate battery state parameters such as SoH and SoC.

## 1.2 Project Background

This thesis is a continuation of the project assignment entitled *Fiber Bragg Grating Optical Sensors for Strain and Temperature Sensing on Lithium-Ion Batteries*. As such, portions of the content within the theory and method chapter have been adapted from the preceding project, elaborated in table 1. This reuse is intended to build upon the foundational research conducted in the pre-project phase, ensuring a coherent progression of ideas and methodologies throughout the exploration of the designated topic. Moreover, this approach allows for a more comprehensive analysis and discussion within the context of the master thesis, offering a deeper understanding of the subject matter. Consequently, listed below is an overview of which sections and to what extent they are reused from the theory and method in the preliminary project.

*Table 1: Overview of reused content from project assignment Fiber Bragg Grating Optical Sensors for Strain and Temperature Sensing on Lithium-Ion Batteries.*

| <b>Section</b> | <b>Description</b>  |
|----------------|---|
| 2.1            | Mostly reused, except the topics of lithium intercalation stages and Coulombic efficiency |
| 2.2            | Mostly reused, except subsection 2.2.5  |
| 2.3            | Reused  |
| 2.4            | Not reused  |
| 2.5            | Not reused  |
| 2.6            | Subsection 2.6.3 and 2.6.4 are mostly reused  |
| 3.1            | Subsection 3.1.1, 3.1.2 and 3.1.3 are mostly reused                                       |
| 3.2            | Section 3.2.1 is partly reused  |
| 3.3            | Partly reused   |
| 3.4            | Not reused  |
| 3.5            | Not reused  |
| 3.6            | Not reused  |
| 3.7            | Not reused  |



---

## 2 Theory

This chapter lays the foundation for theoretical knowledge essential better to understand the results and findings during this research. That is, the complex chemistry of lithium-ion batteries (LIBs) and the theoretical principle and use areas for FBGs. The increase in battery usage for electrical energy storage forces the battery market to evolve rapidly. Both mobile and stationary applications drive the research towards secondary batteries, where LIBs are one of the leading technologies. These sectors require high safety, reliability, and performance, which demands continuous technological improvements for further deployment. [15]

Consequently, a good understanding of the fundamental principles of batteries, material advancements, battery states, and degradation mechanisms is important to comprehend the processes inside the battery during cycling. By combining this knowledge with advanced sensing technologies, particularly optical fiber sensing, valuable data can be extracted that enhances the understanding of battery behavior. This, in turn, paves the way for innovations that can significantly improve battery performance, efficiency, and safety.

This chapter starts by introducing the fundamental principles of lithium-ion batteries, focusing specifically on those using NMC111 and artificial graphite (AG) as cathode and anode materials, respectively. These electrodes are widely studied within the field. Additionally, the chapter will discuss other electrode materials to provide a broader context and enable a comparison of the results presented in this thesis with findings from other studies.

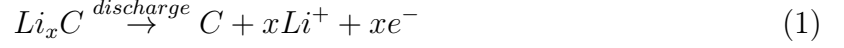
Furthermore, this chapter will discuss the various aspects of battery manufacturing, including assembly, formation, and testing. It will also introduce the analytical tools employed in this study, detailing both the battery state parameters and the advanced sensing technologies used. Notably, fiber Bragg grating optical sensors are a crucial component in the measurement and analysis framework of this research.

### 2.1 Lithium-Ion Batteries

Lithium-ion batteries are complex electrochemical energy carriers, which use the idea of ion intercalation, where lithium ions move back and forth between the negative and positive electrodes. This movement occurs through a conductive electrolyte and a separator that prevents direct contact between the electrodes while allowing ionic flow. During discharge, lithium ions are released from the anode and travel through the electrolyte to the cathode, releasing stored energy in the process. Conversely, during charging, an external electrical power source forces the lithium ions back to the anode, storing energy in the chemical bonds again. [9]

Lithiated carbon ( $Li_xC$ ) and lithium nickel manganese cobalt oxide (NMC111,  $Li_xNi_{\frac{1}{3}}Mn_{\frac{1}{3}}Co_{\frac{1}{3}}O_2$ ) are common anodes and cathodes used in LIBs, respectively. In fully charged batteries, the lithium ions are stored in the negative electrode. During discharge,

a load is applied which leads to the oxidation reaction in the anode, that releases the lithium ions and electrons:



The lithium ions move through the electrolyte and separator to the cathode, while the electrons travel through an external circuit from the anode to the cathode electrode. A schematic of the discharging of a lithium-ion battery is shown in figure 2.1a. The reduction reaction occurs in the positive electrode:

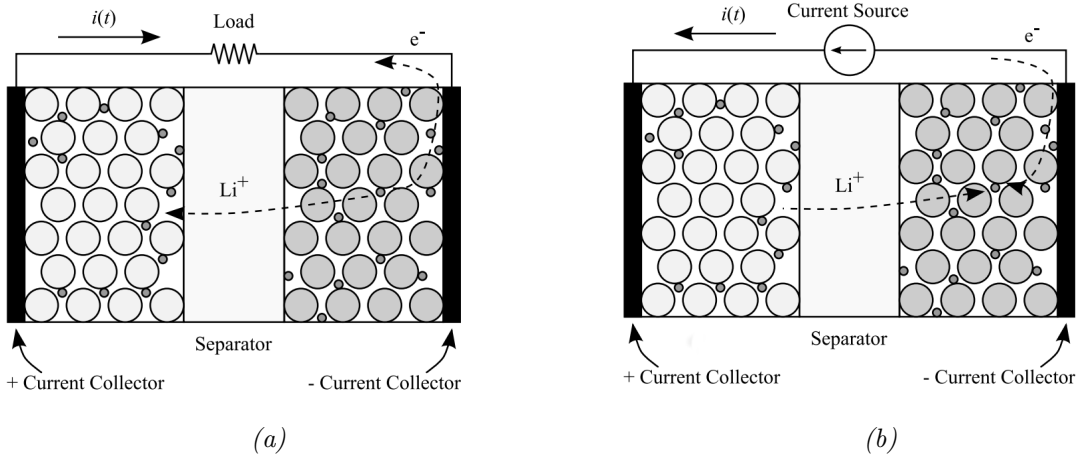
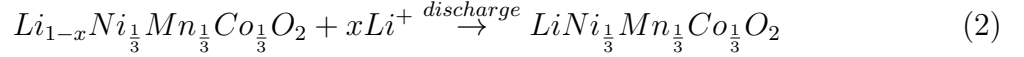
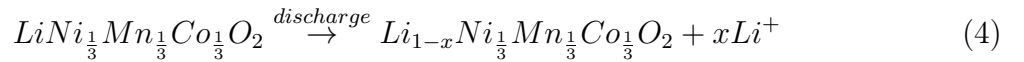


Figure 2.1: a) Discharge and b) charge for a lithium-ion battery. [9]

During charge, an external current source is applied and the reaction is reversed. This forces the current to move from the negative to the positive electrode. As shown in figure 2.1b, the active material in the negative electrode is reduced. Carbon, lithium ions, and electrons react to form lithiated carbon:



While charging, oxidation occurs at the positive electrode, and lithium ions are de-intercalated [9]:



Different lithium intercalation stages occur during the charging process. As lithium intercalates into the graphite anode, lithium-graphite intercalation compounds are formed in different phases,  $Li_xC$  ( $0 < x < 1$ ). In a fully lithiated graphite anode, the structure consists of one lithium atom per six carbons, i.e.  $x = 1$ , giving the structure  $LiC_6$ . This fully intercalated stage gives a specific capacity of 372 mAh/g, when perfectly stacked

[16]. However, in an experimental set-up, this rarely occurs as there is always some form of stacking disorder. The different stages of lithium intercalation occur at specific voltages and are usually separated into four stages shown in figure 2.2. [17]

During the intercalation process, as the lithium concentration increases, phase transitions can occur. At lower concentrations of lithium, the lithium ions intercalate into the hexagonal structure of graphite. The anode maintains a stable structure. With increasing lithium concentration, a rearrangement of the anode can occur, leading to a monoclinic structure. This phase transition is caused by the need to accommodate more lithium ions within the graphite. [18]

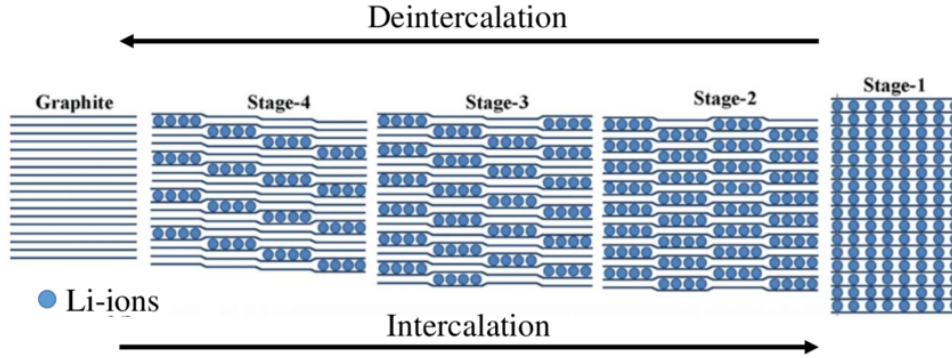


Figure 2.2: Stages of intercalation and de-intercalation in a graphite anode. [19]

Depending on the battery chemistry, the different materials have different electrochemical potentials. The standard reduction potential in a cell can be calculated from the potential of the two half cells:

$$E_{cell}^0 = E_{cat}^0 - E_{an}^0 \quad (5)$$

where  $E_{cell}^0$  is the potential measured when all the components are in standard state,  $E_{cat}^0$  and  $E_{an}^0$  is the standard potential of the cathode and anode, respectively. For a galvanic cell used as a power source, the half-cells are selected based on obtaining a large difference in potential. [20]

A battery is driven by a spontaneous chemical reaction that produces electricity. The maximum reversible work that can be performed by a closed system is called Gibbs free energy ( $\Delta G$ ):

$$\Delta G = \Delta H - T\Delta S \quad (6)$$

where  $\Delta H$  is the enthalpy change,  $T$  is the absolute temperature in kelvin and  $\Delta S$  is the entropy change.  $\Delta H$  can be seen as the theoretically available energy and  $T\Delta S$  can be viewed as the reversible amount of heat consumed or released during the reaction. When the reactions in the electrodes occur spontaneously, the standard free energy (Gibbs free

energy) is negative. Gibbs free energy can also be obtained from the standard reduction potential of the cell:

$$\Delta G = -nFE_{cell}^0 \quad (7)$$

where  $n$  is the number of electrons,  $F$  is Faradays constant and  $E_{cell}^0$  is the standard cell potential calculated in equation 5. [20]

Further, a battery cell rarely operates under standard conditions. The Nernst equation provides a method for calculating the equilibrium potential,  $E_{eq}$  from the standard cell potential  $E_{cell}^0$ , under specific conditions:

$$E_{eq} = E_{cell}^0 - \frac{RT}{nF} \ln(Q) \quad (8)$$

where  $R$  is the gas constant,  $T$  is the temperature in kelvin, and  $Q$  is the reaction quotient of the reactants. Consequently, the Nernst equation shows the dependency of the reactant's concentration and temperature. [20]

Furthermore, the operation and charge transfer in LIBs do not happen at 100% efficiency. There are internal irreversibilities that occur mainly due to ohmic losses ( $IR$ ) and different overpotentials ( $\eta$ ), such as activation overpotential (charge transfer) and concentration overpotential. These factors are accounted for when calculating the real cell voltage,  $E_{cell}$ :

$$E_{cell} = E_{eq} \pm \eta \pm IR \quad (9)$$

where  $\eta$  and  $IR$  are added during charging, as they need to be overcome, but subtracted from  $E_{cell}^0$  when discharged, as they are losses. The effect these losses have on the cell potential when discharged is displayed in figure 2.3. [20]

Further, the efficiency ( $\epsilon$ ) of the charging and discharging process can be calculated:

$$\epsilon_{charge} = \frac{E_{eq}}{E_{cell}^{charge}} \quad (10)$$

$$\epsilon_{discharge} = \frac{E_{cell}^{discharge}}{E_{eq}} \quad (11)$$

and the total round-trip efficiency, also called Coulombic efficiency, can be described as:

$$\epsilon_{total} = \epsilon_{charge} \epsilon_{discharge} \quad (12)$$

The Coulombic efficiency of a cell can be used to monitor the magnitude of unwanted side reactions. A Coulombic efficiency equal to 1 would indicate a fully reversible cell. A substantial amount of research has studied Coulombic efficiency and its relationship with

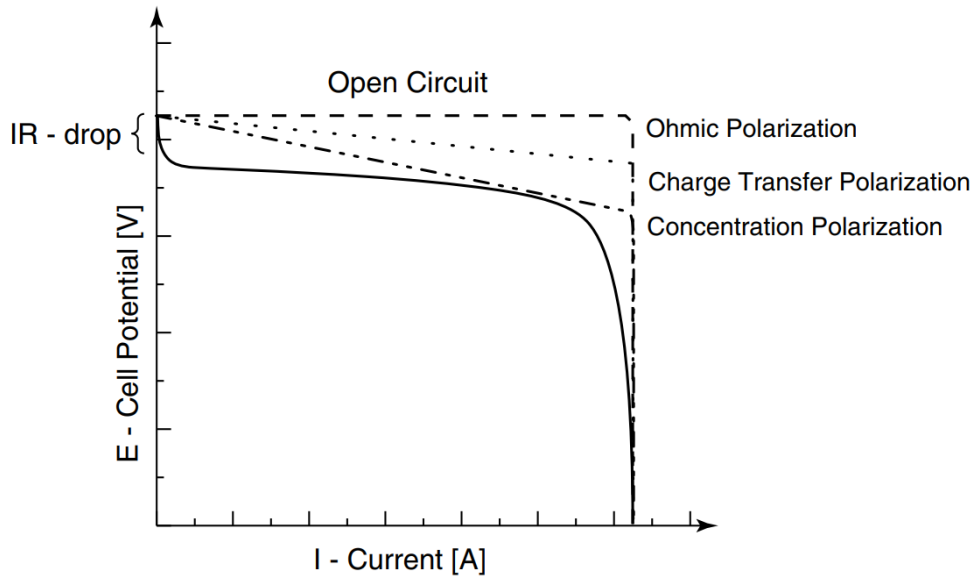


Figure 2.3: Cell polarization as a function of operating current. [20]

other battery parameters such as state of charge and battery lifetime. Yang et al. [21] performed a study exploring the relationship between long-term Coulombic efficiency and battery degradation. They observed a strong relationship between Coulombic efficiency and degradation of the battery. It can be used as an indicator of degradation rate, where a stable Coulombic efficiency curve corresponds to a constant degradation rate. [21, 22]

Irreversible reactions in a cell during cycling cause capacity loss, which can generate heat. If the heat cannot dissipate fast enough, the temperature will increase within the battery cell. If the temperature increase is too high side reactions like increased SEI development, or in the worst case thermal runaway, may occur. This is further elaborated in section 2.5. [23]

## 2.2 Anode and Cathode Materials in Lithium-Ion Batteries

Ongoing research in the field of anode and cathode materials aims to improve the performance, efficiency, and safety of LIBs. Material choice and optimization are crucial for achieving maximum performance and tolerable safety. Lithium is the lightest metal and the most electro-positive element, making it suitable for high energy density storage. Its unique ability to react reversibly with inorganic compounds makes the basis of rechargeable LIBs. [24]

Improving LIB performance depends on the capacity of the cell, making the selection of compatible, high-capacity electrode materials essential. Although many materials offer high theoretical capacities, not all lithium ions can be extracted during de-intercalation without causing structural breakdown of the material. Consequently, the reversible capacity of a material is lower than its theoretical capacity, which must be considered when estimating full cell capacity. [25]

### 2.2.1 Anode Materials

Today, the most commonly used anode material is graphite. However, the market demands high-performance LIBs for several applications, and graphite does not meet all the requirements. Consequently, further research on anode materials is important for the improvement of safety and performance in LIBs. Current trends and research have shifted the market towards lithium alloy metals. [26]

Graphite has a high specific capacity of 372 mAh/g high volumetric capacity, and low cost [16]. The low average voltage is advantageous, however still high enough to avoid lithium plating. Other advantages imply high reversibility, good thermal stability, and good cycle life. Graphite also exhibits relatively low volume variation during cycling, estimated to be 10% [26]. As shown in figure 2.4, graphite consists of sheets arranged in a hexagonal or rhombohedral structure. When lithium ions are inserted, the graphene sheets rearrange, stacking on top of one another, leading to a phenomenon known as 'staging'. In contrast, non-graphitic carbons lack graphene's structural order, leading to higher irreversibility, but their reduced exposure to SEI formation is favorable. Overall, graphite exhibits great properties, and research on improving this material by developing alloy anode materials is a difficult task. [25, 26]

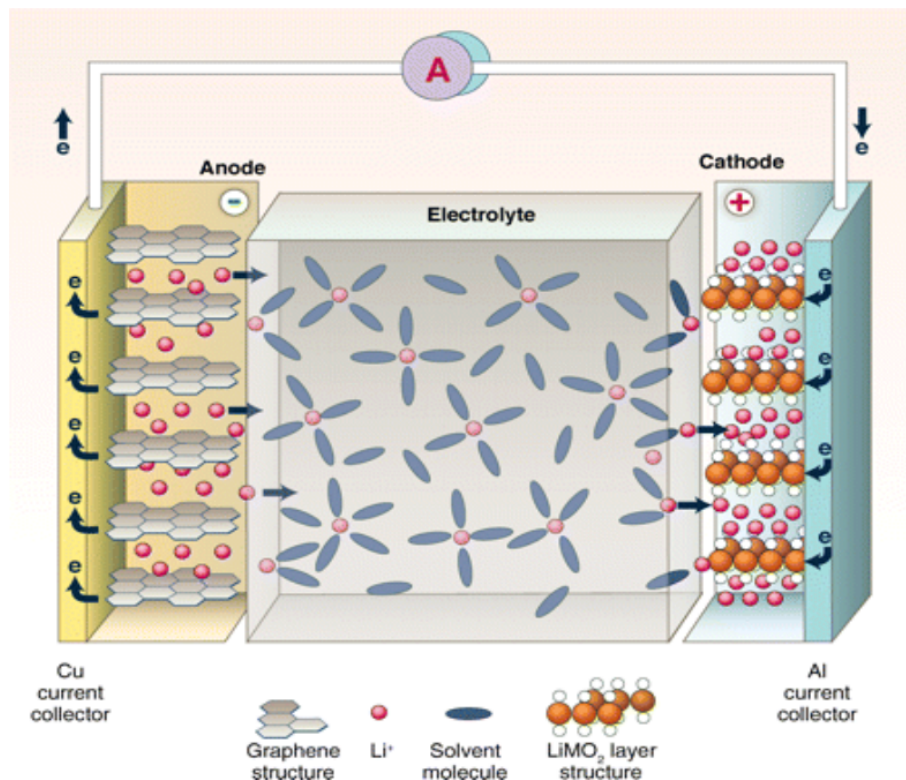


Figure 2.4: Chemical structure of lithium-ion battery. [24]

Lithium alloy anodes are gaining more attention as they show good intercalation capacity. Although they offer improved volumetric and specific capacities over traditional graphite anodes, there are challenges, including lower electrical conductivity and dendrite formation. These drawbacks can cause irreversible capacity losses, reducing performance.

Furthermore, lithium alloys undergo considerable volumetric expansion during lithiation, which poses a risk of mechanical stress and damage to the anode. To ensure a comprehensive understanding of the practical implications of using lithium alloy anodes in batteries, it is crucial to evaluate their volumetric capacity relative to the alloy volume when fully lithiated. This approach provides a more accurate comparison with other anode materials and assists in assessing practical cell performance. [24, 26]

Composite graphite anodes are emerging with favorable features, where silicon is highlighted as a promising material. Silicon is an abundant and inexpensive material, exhibiting favorable characteristics like great gravimetric and volumetric capacities, as well as no safety risks. However, silicon endures substantial volume expansion of up to 300% during cycling, which can cause pulverization of the anode and lead to an unstable SEI layer [27]. This together with poor electrical conductivity is one of the greatest drawbacks of silicon anodes. [26]

The actual lithium capacity of a silicon anode is substantially lower than the theoretical value. This is caused by the recurrent creation of the SEI layer, particle cracking, and ineffective electron transfer. Some challenges need to be solved, such as the low Coulombic efficiency of silicon, especially compared to graphite anodes. However, silicon shows great potential as LIB anode, and with more research in the field, silicon can lead to a significant breakthrough in LIB technology. [26]

### 2.2.2 Cathode Materials

The cathode material serves as the primary source of lithium ions in LIBs. The most common cathode chemistries are lithium manganese oxide (LMO), lithium iron phosphate (LFP), and layered metal oxides such as lithium cobalt oxide (LCO), lithium nickel manganese cobalt oxide (NMC), and lithium nickel cobalt aluminum oxide (NCA). [24]

Layered metal oxides includes LCO, NMC, and NCA. The layered structure of LCO is shown in figure 2.5. Lithiated nickel and cobalt oxides are extensively researched materials for LIBs. Both nickel and cobalt exhibit exceptional structural stability. However, their scarcity poses challenges in manufacturing, making them expensive and challenging to synthesize. All three above-mentioned cathodes exhibit good specific energy. [24]

Mixed transition metals such as  $LiNi_xMn_yCo_{1-x-y}O_2$  were initially suggested to overcome the individual drawbacks of each oxide, such as limited stability, safety concerns, and low specific capacity. Among the different ratio combinations,  $LiNi_{\frac{1}{3}}Mn_{\frac{1}{3}}Co_{\frac{1}{3}}O_2$ , shows highly promising potential, with a specific capacity of 200 mAh/g when charged to 4.6 V vs. Li/Li<sup>+</sup>. NMC also has the advantage of good specific power density, while NCA portrays a good life span. [24, 28]

LMO is a commonly used cathode material, with desirable characteristics such as low cost, good accessibility, and favorable electrochemical properties. The LMO material forms a spinel structure, as shown in figure 2.5, that makes it suitable for the intercalation of small lithium ions. However, the spinel structure causes lower energy density and overall capacity. The structure of the olivine LFP cathodes is shown in figure 2.5. This cathode

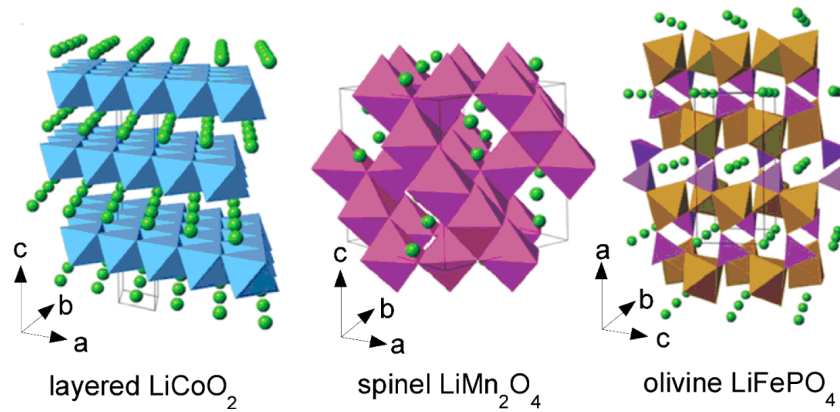


Figure 2.5: Structure of the three lithium-insertion compounds; layered, spinel, and olivine. [29]

is a composite of non-toxic materials and has a good state of health (SoH) throughout the life of the battery. Iron is a cheap and abundant material, as well as environmentally friendly. Compared to other cathode chemistries, LFP experiences less volume expansion and heat flow when cycled. [24, 30]

### 2.2.3 Electrolyte

The electrolyte in a LIB facilitates the movement of lithium ions back and forth during the charging and discharging of the battery. The mobility of the ions in the electrodes affects the power output of the battery and it is mainly determined by the electrochemical reaction in the cell. The SEI layer formation is also affected by the specific electrolyte composition. The electrolyte composition in a LIB consists of a solvent, conductive salt, and additives. The specific composition differs in different batteries and is company-specific. Some desired properties of electrolyte solutions are electrochemical and thermal stability, good solubility, high conductivity, low cost, and non-toxicity. There is ongoing research on advancing the electrolyte to improve ionic conductivity. [20, 24, 30]

### 2.2.4 Separator

The separator's main purpose in a LIB is to act as a barrier between the anode and cathode, while also being permeable to lithium ions. There is a close coherence between the separator and the safety of the battery. High temperature in a battery can cause the separator to break or even burn. This can lead to direct contact between the anode and cathode, resulting in a short circuit of the battery. To enhance the safety of LIBs, the separator should exhibit good mechanical strength to maintain the structure integrity, exceptional heat resistance, and possibly possess flame-retardant properties. It should also possess qualities to limit dendrite growth and show excellent chemical compatibility to prevent reactions between the separator and other battery components. [31]

### 2.2.5 Current Collector

The anode and cathode materials are commonly put onto a current collector. The current collector is an electrically conductive substrate that facilitates the flow of electrons to and



from the external circuit. They are usually made from materials with excellent electricity-conducting abilities. Copper is a commonly used current collector for the anode side and aluminum for the cathode side. [32]

As the current collectors are in contact with the electrolyte, side reactions can occur, leading to surface corrosion. This causes an increase in the contact resistance between the electrode material and the current collector, leading to an increase in ohmic overpotentials. Moreover, corrosion results in the nonuniform distribution of current, facilitating lithium plating. Severe corrosion can cause a loss of contact between the active material and current collector resulting in a decrease in cell capacity. [33, 34]

## 2.3 Battery State Parameters

Despite the several advantages of using LIBs for energy storage, there are still limitations related to the safety and lifetime of the battery. The demand for batteries continues to increase and a reliable battery management system (BMS) is essential to monitor the battery during use. Knowing the state of charge (SoC) is essential to ensure the safety, performance, and lifetime of batteries. To maximize the operation, an efficient model for estimation and monitoring of state of charge, state of health (SoH), and depth of discharge (DoD) is essential. [35, 36]

### 2.3.1 State of Charge

The state of charge of a battery is defined by the available capacity in Ah,  $C_{available}$ . It is a percentage of the momentary maximum capacity,  $C_{max}$ , of the battery:

$$SoC = \frac{C_{available}}{C_{max}} \cdot 100\% \quad (13)$$

SoC indicates how much energy is currently stored in the battery, relative to its full capacity. It can be viewed as a parameter used to assess the potential energy in a battery. To find the residual capacity in a battery, both Coulomb counting and open circuit voltage methods can be used. In the Coulomb method, the charge/discharge current is measured over time to determine the energy. Another method is to measure the open circuit voltage. The difference in electrical potential between two terminals is measured when disconnected from a circuit. A disadvantage of this method is that long-term equilibrium conditions are required. [35]

The depth of discharge can be defined as the released capacity compared to the momentary maximum capacity, expressed as a percentage:

$$DoD = \frac{C_{released}}{C_{max}} \cdot 100\% \quad (14)$$

The SoC is inversely proportional to the DoD:

$$SoC = 100\% - DoD \quad (15)$$

### 2.3.2 State of Health

The state of health of a battery can be defined as the battery's ability to store and deliver energy. It represents the current storage ability compared to a battery in unused condition. It is a difficult parameter to measure because it is not possible to open an operating battery. Therefore it is measured indirectly as the maximum available battery capacity compared to the rated capacity:

$$SoH = \frac{C_{max}}{C_{rated}} 100\% \quad (16)$$

SoH provides insights into how much a battery's capacity has degraded over time. Throughout its life, a battery undergoes natural aging and degradation due to various factors such as charge-discharge cycles, operating conditions, temperature, and the chemistry of the battery. This degradation leads to a reduction in the battery's total capacity. A higher SoH value, close to 100%, indicates that the battery's capacity is still relatively close to its rated capacity, suggesting good health and performance. [35]

### 2.3.3 C-rate

When cycling the battery, the terminal voltage increases and decreases as the current is varied. When fully charged or discharged, the battery voltage stabilizes at a constant level, in correlation to the SoC. SoC is defined to be 100% when the battery is completely charged and 0% when fully discharged. Consequently, in the case of a degraded battery, the SoC for the maximum possible charge is always defined as 100%. By measuring the voltage in the battery during constant current charge/discharge, the dynamics of the battery can be characterized. The rate at which the battery is charged or discharged is measured relative to the battery capacity. It is defined as the power delivered (or drained) from the battery compared to the capacity of the battery [9]:

$$C - rate = \frac{Power}{Capacity} \quad (17)$$

C-rate can also be expressed as a function of SoC:

$$C - rate = \frac{\Delta SoC / hours}{100} \quad (18)$$

The charge acceptance for a battery is the maximum acceptable charge rate. This is due to heat generation and side reactions occurring at high current charging which can affect the battery life. [9]

To cycle a battery at a certain C-rate, the capacity of the battery needs to be known. The capacity of batteries is different due to the use of different materials, manufacturing companies, etc. The theoretical capacity ( $Q_{theoretical}$ ) can be used as an initial guess:

$$Q_{theoretical} = \frac{n \cdot F}{3600 \cdot M} \quad (19)$$

where  $n$  is the number of electrons transferred in the reaction,  $F$  is Faraday's constant and  $M$  is the molecular weight of the active material [9]. The actual capacity usually differs from the theoretical capacity in practical applications but can be calculated from the voltage-time curve obtained during a cycling test. [25]

In practice, the charge/discharge time can differ from the theoretical calculation of dividing capacity by applied current at a certain C-rate. This can be attributed to Peukert's law, which states that as the discharge rate increases, the actual capacity of a battery decreases. Hence, at higher C-rates, a lower effective capacity can be observed. [37]

## 2.4 Battery Manufacturing

Since the lithium-ion battery industry is well-developed today, the main manufacturing steps have been precisely developed. The process can be divided into three main steps, electrode production, cell assembly, and electrochemical activation. Even though companies may have some deviations from each other, the main steps of producing a lithium-ion battery are displayed in figure 2.6.

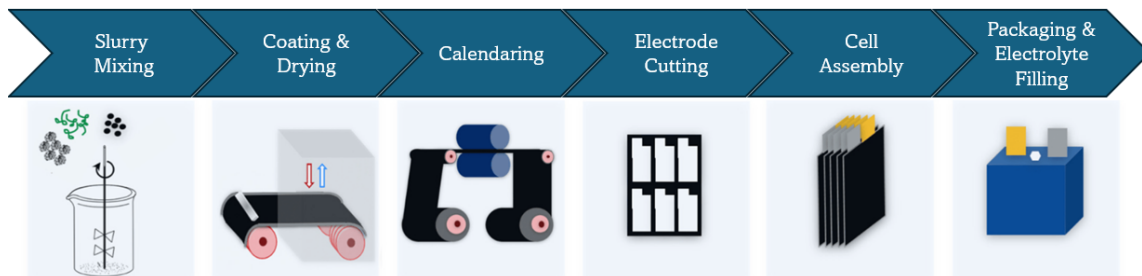


Figure 2.6: Main steps of the battery assembly process (adapted from [38]).

### 2.4.1 Battery Assembly

Firstly the electrodes need to be produced. This is done by mixing the active material with the conductive material binder and additives in a dry mix. Different mixes are made for the negative and positive electrodes, both usually use carbon black as conductive material. After the dry mix is mixed, a solvent is added. The solvent is added to the binder dissolves and mixes with the active and conductive material. [38, 39]

Secondly, the mixed slurry is coated on the current collector, which can be done by slot-die coating, doctor blade coating, or electrostatic spray coating. After the coating process, the coated current collectors are dried, during which the solvent is evaporated. Since the cathode solvent is a toxic material, a recovery process is necessary for the cathode electrode

production. The drying usually happens in dry air or nitrogen conditions, but infrared light or microwaves can also be used. The drying process is important, as it influences the microstructure of the electrodes. After drying, the electrodes are calendared. Calendaring is important as it enhances the conductivity, homogeneity, mechanical strength, elasticity, and adhesion of the electrodes. Then, the finished electrodes are slitted or stamped to the right size for their use, and sent to vacuum drying. [38, 39]

When the electrodes have dried, the cells can be assembled. The internal cell structure is formed as the electrodes and separator are stacked layer by layer. As figure 2.7 shows, there are several different cell geometries for lithium-ion batteries, depending on the application. The most recent assembly method is the pouch cell, but there is also the prismatic, cylindrical, and coin cell. The pouch cell benefits in terms of weight, flexibility, and shape adaptability compared to the more conventional geometries like cylindrical, prismatic, or coin cells. However, the pouch cell has low mechanical resilience and fatigue strength, compared to the others. The coin cell is the cheaper option, as it has few components and production steps. However, it does not apply to high-energy applications. [24, 39]

After the electrodes and separators are stacked and put into their container. The container is filled with electrolytes before it is sealed. Prismatic and cylindrical cells often utilize an aluminum casing sealed by laser welding. Pouch cells are covered in a laminated aluminum foil which is vacuum sealed, while coin cells are sealed through crimping. [24, 38, 39]

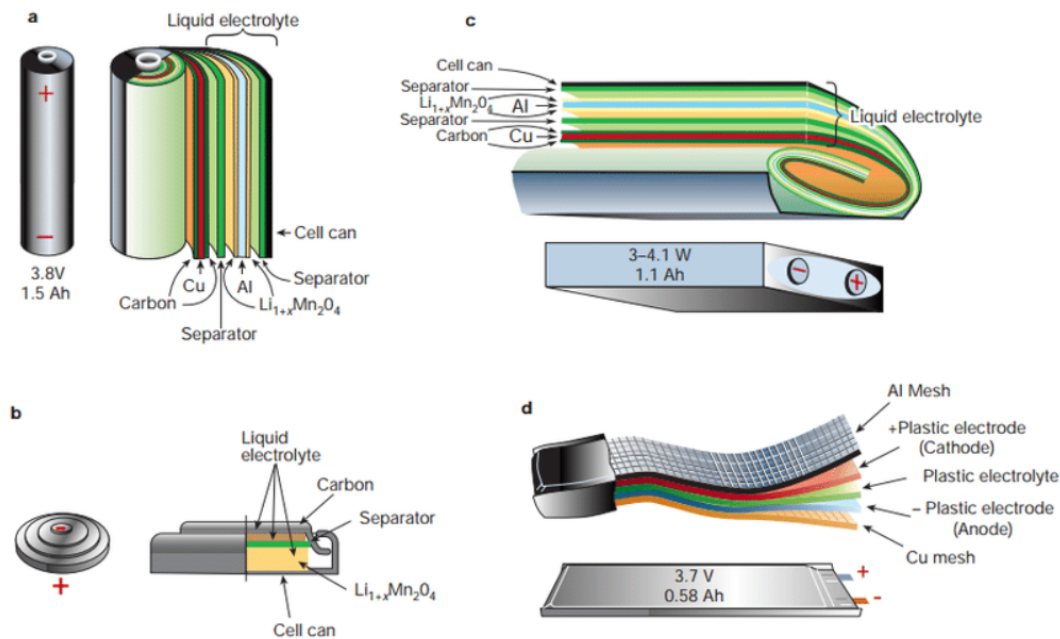


Figure 2.7: Different cell geometries, (a) cylindrical (b) coin (c) prismatic (d) pouch. [24]

When the battery is enclosed, the formation and aging step can take place. Cells can be stored for several weeks to complete the electrolyte wetting and SEI stabilization processes. [38, 39]

### 2.4.2 Formation

The electrolyte wetting, formation, and aging are time-consuming and cost-intensive steps during battery manufacturing. Research is focusing on reducing time and cost without compromising quality and performance. Cell formation and aging is the most expensive step in battery manufacturing, representing about 32% of the total cost [39]. The formation process is important to form a stable SEI layer, as it prevents irreversible consumption of electrolyte and lithium ions, while it protects the anode from overpotential during fast charging. Increasing the C-rate to reduce time consumption is currently being researched. [40, 41]

SEI layer formation occurs in two main steps. Initially, the graphite electrode is polarized, leading to the reductive decomposition of electrolyte components into new chemical species. Subsequently, these decomposition products precipitate, forming the SEI layer, which is complete when it fully covers the graphite surface. The majority of the SEI layer formation occurs during the first lithiation cycle. This irreversible consumption of lithium ions is a significant challenge in LIBs, broadly researched. It results in lower Coulombic efficiency and affects the capacity and longevity of the battery. [7, 42]

To ensure complete saturation of the electrolyte, a rest/wetting step is usually included in the formation schedule. This step affects the performance and safety of the battery. Insufficient electrolyte wetting can reduce the ionic conductivity, due to higher internal resistance, which in turn can lead to reduced capacity. Moreover, incomplete saturation might cause uneven electrolyte distribution within the cell, resulting in local overcharging and possible dendrite formation. Such uneven distribution may also lead to thermal runaway caused by internal hot spots. [43, 44]

It is also common to apply a tap charge to the battery before letting the battery rest for a longer period. This step is intended to increase the voltage of the cell and avoid corrosion of the copper current collector [40]. Further, a rest period for wetting is conducted before the formation cycles can start. The cycling happens under a low charge rate such as C/20 [39]. However, in 2017, An et. al. [45] performed a study on LIB formation processes, where they proposed a fast and effective formation protocol and compared the results with a baseline protocol. The results showed improvement in capacity retention and reduced resistance in the surface film with higher C-rates. Another study performed by Pathan et al. [46], performed ten different active formation protocols, where they concluded that cycling the cell at a higher voltage during formation improves the interface stability of the cell.

After formation, degassing of the cell is often conducted as gas is generated during the formation process. After the discharging of the gas, the cells are stored for aging on shelves. Here, the cells complete the electrolyte wetting and the SEI layer stabilizes. [39]

### 2.4.3 Contamination

Batteries made on research level are often assembled in a glovebox to ensure low levels of water and oxygen in the cell, and to avoid other contaminants from entering the cell

during assembly. A glovebox provides an inert atmosphere that often utilizes high-purity argon or nitrogen gas. LIBs are highly sensitive to water moisture and oxygen, and exposure to this during assembly can cause unwanted chemical reactions and degradation of the battery. This can result in lower performance and safety. A glovebox is designed to keep water and oxygen levels exceptionally low, which is beneficial since water can decompose the electrolyte and react with cathode and anode materials. Avoiding other contaminants entering the battery during assembly is also crucial for the optimization of the battery. Even small particles or contaminants can reduce the longevity and performance of batteries. A controlled environment, such as a glovebox, reduces this risk. [47]

Zheng et al. [48] studied the effect of water contamination on lithium-ion batteries. Some cells were injected with different amounts of deionized water and compared to water-free LIBs. The effects on initial capacity, cycling behavior, voltage, and internal resistance were studied. They concluded that the charging voltage of the first cycle decreased with increasing water content. The initial capacity was also lower, caused by water-related side effects and irreversible lithium loss, as well as the internal resistance variation was higher. They also found that capacity retention rates of 300 cycles were better for water-free batteries. This underlines the importance of assembling the battery in a controlled environment.

Lithium hexafluorophosphate ( $LiPF_6$ ) is the salt most commonly used in electrolyte in secondary LIBs. This salt contains the most essential properties needed in an electrolyte solution. When using a  $LiPF_6$ -based electrolyte, minimizing protic impurities, such as water, is especially important. Water reacts with the electrolyte, causing the formation of hydrofluoric acid. [49]



Hydrofluoric acid can react with the cathode active material, especially the lithium manganese spinel. When water reacts with the electrolyte, it results in irreversible consumption of lithium ions. This demonstrates why capacity decreases with increasing water. [20, 48, 49]

## 2.5 Battery Degradation

Identifying and mitigating degradation mechanisms in LIBs is a difficult task. Many factors, both internal and external, interact and influence battery capacity and longevity. Numerous studies have explored aging and degradation mechanisms and several methods have been investigated to estimate the state of health. However, it is challenging to quantify the different mechanisms as they are correlated and cross-dependant. They are also strongly dependent on operating conditions. The main consequences of degradation in batteries are a decrease in capacity and an increase in resistance. [50]

When a battery is cycled, irreversible reactions occur within the battery. This is caused by

unwanted side reactions and internal resistance. Internal resistance results in ohmic losses, which generate heat and further accelerate degradation processes. The main degradation mechanisms occur in the anode in the form of SEI layer growth, loss of contact due to SEI, corrosion of lithium, and lithium plating. These mechanisms are mostly dependent on temperature, but also on storage and cycling conditions, where the C-rate and the state of charge (SoC) window is of most importance. [9, 51]

### 2.5.1 SEI Layer Formation and Lithium Plating

The main part of the SEI layer forms during formation cycling. However, forming a stable SEI layer is crucial to avoid further unwanted SEI layer growth. A thin, stable SEI layer improves the safety and cycleability of the anode reaction. It prevents irreversible consumption of electrolytes and also protects the anode from overpotential during fast charging. Without a stable SEI layer, irreversible reactions on the electrode surfaces persist and the unstable electrode surface remains exposed to the electrolyte, causing degradation of battery properties. However, excessive SEI formation can influence battery kinetics, particularly rate performance. The SEI layer hinders charge transfer reactions and increases mechanisms the internal resistance. Also, the formation of SEI adsorbs lithium, consequently lowering the battery capacity. Battery operation at too high temperatures is one of the main reasons for SEI layer overgrowth. [7, 51]

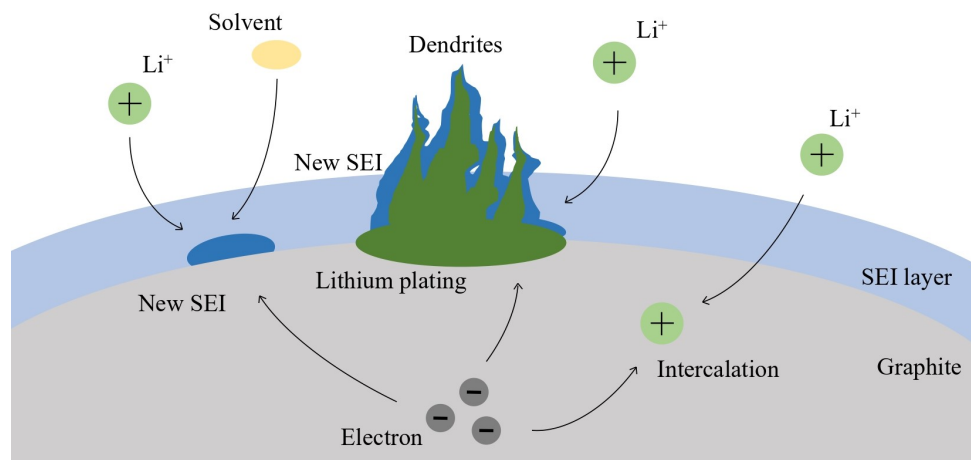


Figure 2.8: SEI layer formation and lithium plating on graphite anode (adapted from [11]).

When operating a battery at low temperatures or during fast charging, the diffusion and migration of ions on the anode can be hindered. This can lead to harmful side reactions, such as lithium plating. Lithium plating can drastically shorten the lifetime of batteries, and limit the charging rate. It occurs when the lithium ions cannot intercalate to the anode fast enough. This leads to the formation of metallic lithium on the anode surface. In the worst case, this metallic lithium can cause lithium dendrites that penetrate the separator, causing internal short circuits and thermal runaway. If the dendrite breaks off before penetrating the separator, the active material is lost to the electrolyte causing a capacity decrease. [51]

### 2.5.2 Surface Polarization and Structural Changes

Upon prolonged cycling of LIBs containing a graphite anode, the anode endures severe structural disordering at the surface. As high lithium ion concentrations occur at the surface during the early stages of cycling, it causes an increase in the  $Li_xC$  spacing. This in turn induces local stress on the edges of the graphite layers and can cause breakage of some of the bonds in the structure. This leaves the edges of the structure exposed and they react with the electrolyte to (re)form the SEI layer. This causes a gradual degradation of the graphite anode as it consumes lithium ions and causes irreversible capacity loss. [17]

High cycling rates can also induce local stress in the graphite lattice, due to high concentration gradients. During the early stages of lithium intercalation, there are high concentrations of lithium ions at the graphite surface and empty inter-layer sites in the graphite bulk. This causes substantial stress on the edges of the graphene layers, possibly resulting in deformation and structural damage. The exposed carbon atoms at the surface will then react with the electrolyte and cause (further) SEI layer growth. [17]

Previous research has shown that lithium ions tend to form stronger bonds with carbon atoms at the graphite edge than in between the layers [52] and that electron transfer rates on the edges are around  $10^5$  times higher than bulk-plane graphite [53]. Lithium ions therefore tend to diffuse toward the edges of the graphite layers, as they are preferentially bound to those sites [52]. This makes the surface concentration of lithium consequently higher than the bulk concentration during intercalation and de-intercalation, especially during the early intercalation stages. The concentration gradient normally diminishes as the process moves towards the later stages of intercalation. As the majority of the unwanted lithium consumption and capacity reduction occurs in the early stages, it is more beneficial to cycle the batteries between later stages. Thus, shallow cycling is beneficial to minimize structural damage and reduce the degradation mechanism occurring in graphite anodes which again improves performance and cycle life. [17]

A study performed by Li et al. [54] investigated the intercalation process of lithium ions, observing expansion, wrinkles, and cracks in the graphite layers. This non-equilibrium behavior degrades the battery and is more distinct at high charging rates. They conclude that the fast accommodation of excessive lithium ions, together with surface polarization is the cause of irreversible structural changes of the graphite anode.

Another study performed by White et al. [55] focuses on the electrochemical intercalation into graphite. They point to irreversible structural changes occurring in the graphite anode during the first intercalation cycle. However, over several de-/intercalation cycles, they observe some of the defects in the structure disappearing, indicating continual dynamic changes in the structure.

### 2.5.3 Thermal Runaway

Thermal runaway is a critical safety concern in LIBs and is characterized by an uncontrolled thermal escalation, leading to potential fire and explosion. The great advantage of the high energy-to-weight ratio of LIBs also results in lower thermal stability. Safety is



a primary concern regarding the further deployment of LIBs. Monitoring and measuring temperature is essential to mitigate these hazards. The main causes of thermal runaway are mechanical, electrical, or thermal abuse. [56]

Wang et al. [56] performed a comparative study on overcharge behavior and thermal runaway in LIBs with different cathode materials. They found that for NMC cathodes, 21.5% of the heat accumulation, leading to thermal runaway, was attributed to charging conditions. Overcharge is a common failure event during the cycling of batteries. During overcharge, there is usually an increase in cell voltage and temperature. This causes an accumulation of heat and gas in the cell. Effects of this can be swelling, thermal runaway, or even fire. During overcharge, the graphite anode cannot accommodate all the lithium ions due to capacity limitations. This can also result in lithium plating on the graphite anode. During lithium plating, dendrites can form, possibly causing internal short circuits. [56]

Both Leising et al. [57] and Saito et al. [58] studied overcharge characterization and behavior, mainly in LCO batteries. They found that the temperature increase in the battery mainly came from ohmic resistance and heat produced by side reactions. As the voltage and temperature increase, the electrolyte will start oxidizing. The thermal decomposition of the anode and cathode, as well as the electrochemical decomposition of the electrolyte, are exothermic reactions. Abusive cycling conditions accelerate these reactions, increasing the heat generated inside the battery. Improved BMSs that detect and prevent overcharging, while monitoring thermal behavior are essential to ensure the safe and reliable operation of LIBs. [56]

Additionally, Cui et al. [12] conducted experiments on NMC/graphite and LFP/graphite batteries in 2023 to find early indicators for the thermal runaway. They categorized thermal runaway into four phases, where the first stage was heat causing the cell to swell due to internal gas generation. This could further lead to thermal runaway and in the worst case fire and explosions.

#### 2.5.4 Gas Formation

Gas formation arises from different sources in LIBs during cycling, such as decomposition of electrolyte solvents at the anode and cathode, as well as structural release from cathode materials. Formation of ethylene, hydrogen ( $H_2$ ), carbon monoxide (CO), and carbon dioxide ( $CO_2$ ), are among the most common gases that form during battery cycling. Hydrogen and ethylene are highly flammable gases and can lead to thermal runaway. Additionally, gas formation can impact cell performance; it is associated with electrode degradation, reduced longevity, electrolyte displacement, and increased cell resistance. The generation of these gases increases the internal pressure in the battery, which causes the cell to swell. There are several ways to obtain data about this gas formation, like analyzing the cell thickness, using Archimedes' laws with in-situ measurements, or utilizing fiber optic sensors. [8]

In a graphite anode, the dominant gas-producing reaction occurring is through the devel-

opment of the SEI layer. The electrolyte reduction reaction causes ethylene production, which occurs from 0.8 V vs. Li/Li<sup>+</sup> until the end of charging. As the SEI layer increases, the electrolyte reduction is limited and the production of ethylene gas is reduced. The first cycle has the highest production of ethylene. Throughout the formation cycling, the SEI layer forms and stabilizes. Due to the gas formation during formation cycling, battery cells are usually degassed after formation. There is significantly less gas formation during normal cycling. [59]

Another source of gas evolution is electrolyte contamination. Specifically, water contamination is the cause of several gas-producing reactions. The reduction of water produces hydrogen gas and hydroxide ions. The hydroxide ions formed during water reduction have been observed to react with EC forming CO<sub>2</sub> gas. Water has also been observed to undergo a hydrolysis reaction with EC. [59]

At the cathode, gas evolution usually occurs from electrolyte oxidation and surface contaminants. Regarding NMC cathodes, gas formation is commonly caused by the decomposition of lithium carbonate, Li<sub>2</sub>CO<sub>3</sub>, on the cathode surface both during manufacturing and storage. CO<sub>2</sub> gas evolution occurs during the decomposition of lithium carbonate from an onset potential of around 3.8 V vs. Li/Li<sup>+</sup>. Removal of Li<sub>2</sub>CO<sub>3</sub> from the NMC cathode is important since the nickel-containing electrodes have such high CO<sub>2</sub> production compared to other electrodes. [59]

Looking at the full cell is essential for understanding gas evolution in LIBs. The gas produced by one electrode is sometimes consumed by the other and reaction products diffusing between the electrodes can initiate parasitic reactions. In a full cell containing a graphite anode, the graphite can act as a sink for the CO<sub>2</sub> produced during the oxidation reaction at the cathode. Xiong et al. [60] showed that the gas formation was significantly reduced when lithiated NMC cathodes were stored with graphite anodes. Ellis et al. [61] injected pouch cells with various gases to examine gas consumption. CO<sub>2</sub> was found to have the highest consumption rate, especially in the presence of delithiated graphite. The magnitude of gas formation in a cell is heavily reliant on the materials of the electrodes, as there are varying cross effects. [59]

## 2.6 Sensing in Batteries

The pursuit of enhancing the quality, reliability, longevity, and safety of LIBs, intensifies the demand for advanced sensing technologies. Traditional BMSs are equipped with robust devices for measuring basic parameters such as voltage, current, and temperature. However, existing monitoring methods reveal a significant gap, especially in accurately assessing strain and precise internal temperature measurements, which are indicators for SoC, SoH, and battery malfunctioning. [62]

### 2.6.1 Thermal Sensing Techniques for LIBs

Temperature measurements of LIBs can be divided into three methods: contact sensors, nondestructive testing, and signal processing. Thermocouples, micro-thermistors, resis-

tance temperature detectors (RTD), and optical fibers are typical contact sensors employed to monitor internal and/or external battery temperature. Non-destructive testing is contactless sensors used to measure internal temperature indirectly. Electrochemical impedance spectroscopy (EIS) and Johnson noise thermometry (JNT) are the most common types of contactless sensors used in the battery industry. Contactless sensors are still at the research level, meaning they have not yet been employed at an industrial scale. Signal processing methods are techniques that rely on measurable signals such as current, voltage, and surface temperature to estimate the internal temperature of batteries. [63–65]

Among contact sensors, thermocouples are widely used in industry due to their advantages of low cost, a wide temperature range (typically -200 to 2500 °C, depending on the type), fast response, and robustness. In batteries, they are utilized to measure both external and internal temperatures. However, since thermocouples are made of two dissimilar metals, they are susceptible to corrosion over time, affecting their accuracy. Additionally, thermocouples traditionally have an inaccuracy of  $\pm 1\text{--}2$  °C due to the need for a reference temperature and their metallurgical properties. They are also prone to electromagnetic interference, leading to substantial inaccuracies. [63, 66]

Thermistors are thermally sensitive resistors that measure temperature by utilizing the variable resistance that responds to the surrounding temperature. They can have either negative temperature coefficients (NTC) or positive temperature coefficients (PTC), meaning the resistance within the thermistor decreases or increases with temperature, respectively. NTC thermistors are more commonly used for temperature measurement. Thermistors are advantageous due to their high-temperature sensitivity, good temperature range (-55 to 300 °C), small size, and low cost. Although they can be unstable, advancements have improved their stability, achieving an accuracy of  $\pm 0.1$  to 1 °C. [65]

Resistance temperature detectors (RTDs) measure temperature by utilizing the increasing resistance within metallic conductors. Although RTDs can be made from various metals, platinum is commonly used due to its advantageous properties. RTDs exhibit a nearly linear relationship with temperature, which simplifies calibration and improves precision. They offer high accuracy (typically  $\pm 0.2\text{--}2$  °C depending on the specific sensor and application), stability, and a wide operational range (-260 to 960 °C). RTDs are predominantly used for external temperature measurements but can also be adapted for internal measurements, though design constraints may sometimes pose challenges. [65]

### 2.6.2 Volume Expansion Sensing Techniques for LIBs

Expansion measurements of LIBs have been suggested as a feasible method for detecting battery malfunctioning, important state parameters, and the quality and homogeneity of batteries. Volume expansion techniques for LIBs can be divided into contact and non-contact sensors. Contact sensors include electrochemical dilatometry (ECD), buoyancy measurements, and strain measurements with FBGs and strain gauges. Non-contact sensors include radiological techniques, like X-ray, to visualize the inner components of LIBs. Additionally optical imaging, like laser displacement, and more. [10, 67]

Mechanical dilatometry is one of the oldest and most used methods for measuring volume expansion of materials. Typical dilatometers include push-piston, push-rod, capacitance dilatometers, high-resolution laser dilatometers, and optical dilatometers. However, for measuring electrochemical devices, such as LIBs, push-piston dilatometers are the most used type. ECD is a powerful tool that can be used for detecting very small expansions of LIB, i.e. SEI layer formation, gassing, lithium plating, etc. Further, it is easy to take into use and needs little post-measurement processing. However, dilatometries are bulky, which will restrain them from being implemented into mobile batteries like those in EVs. [67, 68]

Buoyancy measurements use the ideas of Archimedes law to measure the volume changes of a body. This method can be used for batteries even though it includes submerging the battery in a fluid. Consequently, the fluid must be non-reactive. The method is precise for detecting changes in volume and the setup is relatively cost-effective and the method is straightforward. However, it is sensitive to the surrounding environment, and the nature of the setup restrains it to mainly research purposes, but may also be used for stationary applications. [67]

Laser displacement sensors have emerged as a critical tool for non-contact measurement of battery expansion. These sensors operate based on the triangulation method, where a laser beam is directed at the battery surface, and the reflected beam is captured to measure displacement. The high precision and non-invasive nature of laser displacement sensors make them ideal for real-time monitoring during battery cycling. They can detect minor changes in the battery's dimensions, providing valuable data on important battery parameters such as intercalation stages of electrodes, and lithium plating. However, the requirement for a clear line of sight and potential sensitivity to environmental conditions are notable limitations. [67, 69]

Optical fiber sensors are sensitive to both temperature and strain, with fiber Bragg grating (FBG) sensors being the most common type used in the battery industry. FBG sensors offer high sensitivity to strain and temperature, and their ability for dual-parameter sensing makes them particularly well-suited for monitoring the complex dynamics within LIBs. Unlike traditional sensors, FBGs can be integrated directly into the cell structure, providing accurate real-time data from within the battery. This capability represents a significant advancement in battery technology, enabling more precise control over battery operation, enhancing safety measures, and potentially extending the operational lifespan of batteries. However, they are sensitive to environmental conditions, which may cause problems in mobile applications. [4, 63, 67]

### 2.6.3 Optical Fiber Sensors

Optical fiber sensors represent a technology that harnesses the interaction between light and matter through mechanisms such as scattering, diffraction, and absorption. As light waves traverse through a medium, they undergo shifts in wavelength and frequency, as well as changes in phase, polarization, and intensity. [4]

Optical fiber sensors have a range of advantages, including geometric versatility and sensitivity compared to traditional techniques. This flexibility enables the construction of devices that can sense diverse physical parameters such as temperature and strain. In addition, they are inert to electromagnetic interference, which extends their utility, making them suitable for deployment in challenging environments characterized by high voltages, electrically noisy, high temperature, and corrosive conditions. [70]

An essential aspect of optical fiber sensor technology is its capability to gather and transmit data from remote or challenging locations using the optical fibers themselves, offering a common technological base for various sensing applications. As light interacts with the fiber, or devices attached to it, alterations in intensity or phase occur, providing valuable information about the environment. This interaction has been harnessed in more than 60 different sensor types, broadly categorized as amplitude or phase (interferometric) sensors. [70]

Amplitude sensors modulate light intensity, known for their simplicity of construction and compatibility with multi-mode fiber technology. However, phase sensors, particularly interferometric ones, offer theoretically heightened sensitivity, demonstrating an improvement of orders of magnitude over existing technologies. [70]

Research suggests that fiber optic sensors are expected to be one of the leading methods used to procure battery parameters. This is specifically due to the multiplexing capabilities that fiber optics have, enabling the possibility to obtain multiple measurements from a single fiber optic sensor. [4, 71]

While the technology is promising, challenges persist in areas such as noise sources, detection processes, packaging, and fiber coatings. Ongoing efforts are directed toward addressing these challenges to fully exploit the potential of optical fiber sensor technology. [70]

#### 2.6.4 Fiber Bragg Grating Sensors

The fiber Bragg grating optical sensor is a type of optical fiber phase sensor that has obtained attention within the field of battery monitoring. FBG sensors employ gratings along the length of an optical fiber. The individual FBGs are fabricated by inducing indivisible, permanent periodic refractive index alterations. When light passes through the Bragg grating, a wavelength, called the Bragg wavelength ( $\lambda_B$ ) is reflected back, while the rest of the light spectrum continues unaffected. This reflected Bragg wavelength changes as a function of several parameters such as strain and temperature among other things. Hence, by analyzing the change in the Bragg wavelength, precise measurements can be obtained related to temperature and strain. [4, 62]

One of the main advantages of an FBG optical fiber is the ability to multiplex along the same optical fiber, which makes it possible to make simultaneous measurements of different parameters. [4, 62]

The Bragg wavelength,  $\lambda_B$ , is expressed as follows:

$$\lambda_B = 2n_{eff}\Lambda \quad (21)$$

where  $n_{eff}$  is the effective refractive index and  $\Lambda$  is the grating period. When a fiber is somehow compressed or extended, alterations in one of these parameters occur, which then culminates in a change in the reflected Bragg wavelength. This is the working principle of FBG sensors. [72]

Information can be obtained about the change in temperature and strain by differentiating equation 21 for  $T$  and  $\epsilon$ . The effects of temperature can be expressed as:

$$\Delta\lambda_T = 2\lambda_B \left( \frac{1}{n_{eff}} \frac{\delta n_{eff}}{\delta T} + \frac{1}{\Lambda} \frac{\delta \Lambda}{\delta T} \right) \Delta T = \lambda_B(\alpha + \xi)\Delta T = K_T\Delta T \quad (22)$$

where  $\alpha$  is the thermal expansion coefficient,  $\xi$  is the thermo-optic coefficient and  $K_T$  is a combination of these, which represents the temperature sensitivity of the FBG.

Figure 2.9 displays the wavelength shift that temperature and strain variations have on the Bragg wavelength. FBGs have a wavelength shift sensitivity typically ranging from 10-13.7 pm/ $^{\circ}$ C [73, 74]. As a result, it is important to calibrate each FBG individually, to find the respective temperature sensitivity. This can easily be done by changing the temperature in a controlled environment. Further, the strain effect on the FBGs can be expressed as:

$$\Delta\lambda_{\epsilon} = \lambda_B \left( \frac{1}{n_{eff}} \frac{\delta n_{eff}}{\delta \epsilon} + \frac{1}{\Lambda} \frac{\delta \Lambda}{\delta \epsilon} \right) \Delta \epsilon = \lambda_B(1 - p_e)\Delta \epsilon = K_{\epsilon}\Delta \epsilon \quad (23)$$

where  $p_e$  is the photoelastic constant of the fiber ( $\approx 0.22$ ) and  $\Delta \epsilon$  is the applied strain. The fiber's sensitivity to strain,  $K_{\epsilon}$ , is approximately 1.2 pm/ $\mu\epsilon$  [74]. [72]

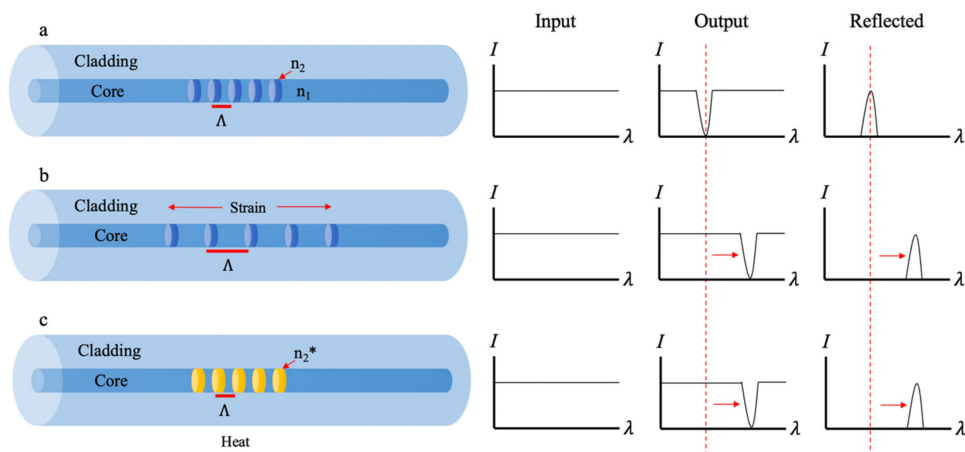


Figure 2.9: Working principle of FBG. (a) An FBG with no effect from strain or heat; (b) Strain-affected FBG, changing the grating spacing, causing a shift in the Bragg wavelength; (c) Heat-affected FBG where the wavelength shifts as the effective refractive index of the gratings change. [73]

Several literature studies have been published for strain and temperature measurements with FBGs to predict the SoC and SoH of batteries. In the context of batteries, FBG sensing networks can be categorized into internal and external setups. External sensing was first conducted by Yang et al. [13] in 2013 where FBGs were used for real-time external temperature monitoring on coin batteries. On the other hand, internal monitoring involves embedding fibers within the cell, a technique first used by Bae et al. [75] in 2016. Despite the potential of embedded FBG sensors, there are challenges with electrolyte leakage at the point where the FBGs enter the cell.

### 2.6.5 External Temperature Monitoring

As mentioned, in 2013 Yang et al. [13] were the first to use FBGs for external temperature measurements on LIBs. In this study, FBGs were affixed to the surface of lithium-ion coin cells together with thermocouples. Conductive gel was used to minimize the strain response as well as gaps between the FBGs and the battery surface. The batteries were subject to cycling under normal conditions at 0.1C, followed by abusive conditions such as overcharging and external short circuits. It was concluded that the sensors showed good thermal response in both normal and abusive conditions when compared to thermocouples.

Subsequent research by Nascimento et al. [76] in 2017 enhanced this methodology by employing three FBGs alongside thermocouples to monitor the external real-time temperature of a LIB. This study also confirmed that FBGs provide better results than thermocouples in rise time and resolution under both normal and abnormal conditions. Additionally, FBGs were identified as promising tools for failure detection and useful in BMSs to uncover faulty batteries, particularly in harsh operating environments.

The advantages of using FBGs for temperature measurements are substantiated by a study performed by Huang et al. [77] in 2023. They performed real-time measurements of surface temperature distribution on a pouch cell, where they observed a highly consistent temperature evolution with voltage and current variations during cycling.

### 2.6.6 Strain Monitoring

Strain is another crucial parameter to monitor as it provides more insight into the reactions occurring inside the cell. The mechanical stress induced on the cell can significantly affect battery performance and longevity. Strain monitoring can assist in detecting structural changes and potential failures in batteries. By understanding how the cell expands and contracts during various cycling conditions, strain monitoring can be used to enhance battery operation and management. [78]

In 2015, Meyer et al. [10] concluded that externally mounted FBGs used for strain sensing could detect malfunctioning batteries due to overcharging, gassing, and thermal runaway with up to 50 times higher sensitivity than that of the FBG temperature sensor. They suggested that BMSs that monitor surface strain can enhance the safety of LIBs and that thermal runaways can be avoided. Moreover, they proposed that the FBGs could be used to estimate SoH as volume change behavior can be related to battery age.

Further, in 2019, Peng et al. [79] explored the relationship between strain and SoC using FBG sensors with high-precision strain monitoring. They developed a sensitization structure that includes a lever amplification and a flexure hinge to more accurately measure external strain. These sensors showed higher sensitivity than bare fiber sensors and stronger disturbance resistance. They found a clear correlation between strain and SoC, showing the same strain evolution profile for different C-rates.

As external measurements reflect the total induced stress on the surface, internal measurements can capture more subtle deformations and stresses within the cell. Bae et al. [75] performed a study examining internal strain measurements by using FBG sensors. Two different configurations are explored, one where the FBG is attached to the anode surface and one where it is implanted in the anode material. They conclude that the implanted FBG shows better detection sensitivity. However, the implanted FBG measures both longitudinal and transverse strains, whereas where the attached FBG can only measure the axial strain. They further conclude that FBGs can be used to monitor strain evolution during extended battery testing.

### 2.6.7 Dual-Parameter Measurements

One of the noteworthy advantages of FBGs is the ability for dual-parameter measurements, where simultaneous measurements of temperature and strain are broadly researched. As there is a close coherence between strain, temperature, and SoC of a battery, these profiles can be utilized to estimate battery state parameters. This was done by Ee et al. [80], where FBG sensors were used to simultaneously measure strain and temperature on the surface of LFP pouch cells. They improved the accuracy using the Pseudohigh-Resolution interrogation method and estimated SoC utilizing a deep neural network.

Research suggests that FBG sensors are a promising sensing technique, that shows noteworthy strengths such as the adaptability to complex systems. Fibre optic sensors can measure both the external and internal state of a battery. Ganguli et al. [81] monitored the internal state of a pouch cell by embedding FBGs into the cell. This research illustrated how the FBG wavelength shifts in correlation to the state of charge and depth of discharge of the cell. Peng et al. [2] also conducted research that utilized FBG sensors to estimate SoC and SoH. They concluded that using FBG sensors for strain monitoring is an effective tool for real-time state estimation of LIBs, facilitating improved performance and safety of batteries. [80]

In a recent study from 2024, Zhang et al. [27] investigated different particle sizes of silicon electrodes, as well as how stress evolution over time affected the capacity. Both internal and external FBG sensors were used, and they concluded that the strain evolution inside the cell was close to identical to the external strain evolution. However, this study was performed on silicon alloy anodes, which endure severe volume expansion compared to graphite anodes. This study suggests that invasive internal measurements can be replaced by external measurements using FBGs, at least for silicon-based anodes.

As the wavelength returned from the FBG is affected by both strain and temperature, a



decoupling of these parameters is necessary. As thermal runaway is a major safety concern in LIBs, many previous studies focus on thermal measurements in LIBs and how different sensing methods can improve the BMS to ensure safety and enhanced performance. The most common method to obtain temperature measurements when working with FBGs is by the use of micro-tubing, which allows for the optical fiber sensor to expand and contract as a cause of temperature, without inducing strain on the FBG sensors. [82]

Further, Li et al. [83] developed a hinged differential lever sensitization structure that was used for strain sensing together with an FBG sensor to facilitate simultaneous measurement of temperature and strain. The study found that the strain on the battery surface correlates with electrochemical changes and thermal expansion during charge and discharge. The strain on the surface was higher during charge than discharge, and thermal expansion was the main cause of strain change.

The set-up used in the study of Ee et al. [80], as previously introduced, consists of two FBG gratings attached to the surface of the battery. One FBG is fixed on both sides to ensure strain sensitivity. The other FBG is loosely attached so that it is only sensitive to the surface temperature and not influenced by strain.

A similar setup was used by Nascimento et al. [72] in 2018, where a network of five FBGs was glued to a prismatic LIB to simultaneously monitor the temperature and bi-directional strain variation. To obtain these measurements four FBGs were attached to the surface of a cell, two in the y-direction, two in the x-direction, and one FBG measuring the external room temperature. The study found that cycling at high charge and discharge rates increases the strain and temperature variations. They also found that throughout the constant current charge, the maximum strain and temperature occurred at the end of the charge process. The set-up presented proved to be a successful method for simultaneous measurements of strain and temperature providing accurate results. Thermal paste was used in the experiment to enhance thermal conductivity.

The reference sensor method is a well-established method to isolate mechanical from thermal strain sensed by the FBG sensors. This method utilizes a secondary FBG that is unaffected by strain, in addition to the primary FBG that measures both strain and temperature. The secondary FBG is placed in the same thermal environment as the primary FBG. The method compensates for temperature variation by using the secondary strain-free FBG to measure only temperature variations. Then by subtracting this temperature-induced wavelength shift from the total wavelength shift of the primary FBG, the strain-induced wavelength shift can be obtained. [6]

Overall, FBG sensors have emerged as a promising sensing technology, noted for their adaptability in complex systems and unique ability to perform dual-parameter measurements. A good method to decouple strain and temperature is paramount for the utilization of this attribute. FBGs present a broad application field and hold immense potential for advancing temperature, and strain measurements within battery monitoring systems. As research continues to refine these applications, the integration of FBGs could become a standard practice for ensuring the safety and efficiency of future battery technologies.

---

## 3 Method

The main framework of this thesis is illustrated in figure 3.1. The details of each step are further elaborated in this section. The thesis objective of the thesis is to evaluate the use of fiber Bragg grating optical sensors for real-time monitoring of NMC111/graphite coin cells. Externally mounted FBGs obtained strain and temperature measurements on the battery on the battery surface during formation, normal, and abusive cycling. Further, utilizing external strain measurements from FBGs to estimate battery state parameters such as SoH and SoC are examined, as well as their ability to detect battery failure.

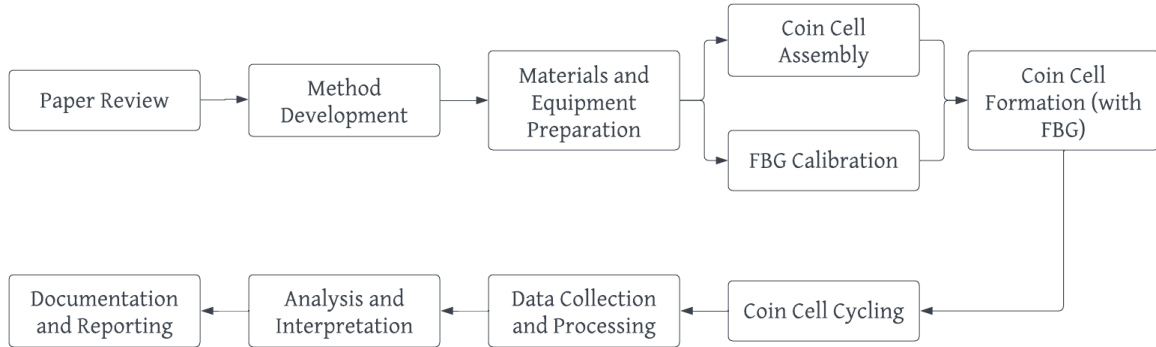


Figure 3.1: Project method.

### 3.1 Materials and Equipment

The battery materials used in the project are commonly used commercial anode, cathode, separator, and electrolyte, convenient for relating the results to previous research and literature. The materials used in the coin cells are chosen to obtain a basis for comparison with literature studies. This section gives an overview of the materials and equipment used in this thesis.

#### 3.1.1 Electrodes

The electrodes used in the coin cells are NMC111 as the cathode and artificial graphite (AG) as the anode. The NMC111 cathode has an active material ratio of 96.4% and a coating weight of 15 mg/cm<sup>2</sup>. The AG anode has an active material ratio of 95.7% and a coating weight of 7.7 mg/cm<sup>2</sup>. For the coin cell assembly, discs with a diameter of 15 mm were punched from manufactured electrode sheets. The anode and cathode electrodes were punched with the same punching size, due to the lack of smaller sizes.

The NMC111 cathode and graphite anode have a specific theoretical capacity of respectively 200 mAh/g [28] and 372 mAh/g [25]. Both electrodes, punched to the same size, have a cross-sectional area of 1.77 cm<sup>2</sup>. The theoretical capacity can be calculated for each electrode using the active material ratio, coating weight, and cross-sectional area, together with the specific capacity of the respective electrodes.

### 3.1.2 Electrolyte

The electrolyte used in the coin cells was lithium hexafluorophosphate solution, with a 50/50 EC/EMC composition. The coin cells were filled with 50  $\mu\text{l}$  of this solution.

### 3.1.3 Separators

The separator used for the coin cell was a Celgard trilayer membrane (PP/PE/PP), which was punched the same way as the electrodes, but with a diameter of 17 mm. The separator needs to be bigger than the electrodes to avoid an internal short circuit.

### 3.1.4 FBG Sensors

During cycling, FBG sensors were attached to the coin cell surface, at the cathode side, to measure temperature and strain. The FBG sensors used in this project were 2-array FBGs and single FBGs from AtGrating Technologies, with a central wavelength of 1530 and 1540 nm. The fiber type in these sensors is Fibercore Polyimide SM fiber. Two FBGs were used simultaneously, to be able to decouple the parameters affecting the wavelength. Detailed information about the FBG sensors can be found in Appendix A.

## 3.2 Coin Cell Assembly

The coin cell assembling process is a crucial part of the study, as it critically affects battery performance during testing. The assembly was performed in a controlled environment to ensure precision and reproducibility. The specific challenges encountered during the initial phases are outlined, including the adjustments made to optimize the procedure and mitigate potential sources of error. This methodical approach was chosen to achieve consistent and reliable results.

### 3.2.1 Material Preparation and Assembly

The coin cells used in this study were assembled in a controlled environment using a glove box (LABMASTER Pro SP, MBRAUN) to ensure minimal contamination from impurities such as oxygen and hydrogen. The assembly components, including electrodes, separator, electrolyte, and casing, were all commercially sourced. The electrodes and separators were subjected to preliminary vacuum drying to eliminate potential contaminants before being transferred to the glove box.

For the cell assembly, the casing used was a LIR2032 made of aluminum. Assembly began with a single drop of electrolyte in the middle of the positive case, facilitating the correct placement of the NMC111 cathode. Subsequently, a total of 50  $\mu\text{l}$  of electrolyte was added. This was followed by the placement of the separator, the AG anode, then a spacer, and a spring, before the negative case was placed on top. The assembly process was completed with the sealing of the cell using a hydraulic crimper (MSK-PN110-S) inside the glove box. An illustration of the assembly is depicted in figure 3.2.

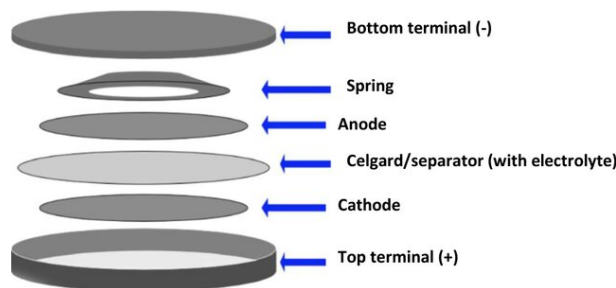


Figure 3.2: Schematic of coin cell assembly. [84]

### 3.2.2 Challenges, Adjustments and Sources of Error

During the initial weeks of experimentation, several challenges were encountered, such as inconsistent cell performance and potential internal short circuits during the crimping process. Troubleshooting efforts revealed two primary issues: contamination of the electrolyte and oversized electrodes and separators. To address these issues, the electrolyte was changed, and the diameters of the electrodes and separators were adjusted from 17mm and 19mm to 15mm and 17mm, respectively. The adjustment helped mitigate the risk of short circuits and improved the assembly process.

Throughout the project, the efficiency and success rate of the coin cells gradually improved. The substantial initial variability in performance was attributed to the excessive dimensions of the electrodes and electrolyte contamination. Notably, the anode graphite electrodes were particularly susceptible to detaching small parts of the active material from the current collector. This occurred primarily around the edges, reducing the active material surface area and thereby capacity of the electrodes.

Moreover, the crimping process occasionally led to deformations in the external casing of the cells, likely caused by dried electrolyte salt in the crimper. Cells exhibiting obvious deformations were excluded from subsequent experiments. However, minor undetected deformations may have contributed to varying results during the project. Additional sources of error were identified, including slight variations in electrodes due to damage from punching and rough handling, residual air impurities within the glove box (which cannot be completely eliminated), and slight discrepancies in electrolyte volume, all of which could influence the overall performance of the cells.

## 3.3 Formation Cycle

Formation cycling is the next step after cell assembly. The formation protocol in this study involved cycling the coin cells at a rate of C/10. The C-rate was established as the average C/10 capacity of 10 well-working coin cells, after formation cycling. However, the theoretical value can be used as an initial guess and indicator of how high the actual capacity should be. The cells were set to formation cycling relatively quickly after assembly.

To ensure complete saturation of the electrolyte within the separator and electrodes, two rest periods were implemented. The cell initially rested for two hours. Given that the

anode current collector is composed of copper, an initial tap charge was applied to prevent corrosion. This tap charge involved raising the battery voltage to 1.5 V through a constant current (CC) charge of C/100, then maintaining the cell at a constant voltage (CV) of 1.5 V for 4 hours, followed by a 12-hour rest period. Subsequently, the cells were charged to 4.2 V and discharged to 3V. This was done a total of five times. A 20-hour cut-off was applied because the initial cycle often struggled to reach 4.2 V. However, discharging the battery to 3 V and recharging to 4.2 V showed promising results.

The raw data obtained from the formation cycling of the cells reflect the performance of the batteries. Some batteries showed poor characteristics, and the whole process of the assembly was repeated to obtain higher-quality batteries. After several attempts, to test different formation schedules, the batteries showed varying capacities and performance.

### 3.4 Coin Cell Cycling

After formation, the coin cells were subjected to various cycling schedules, with FBGs attached to the cell surface to monitor performance and detect potential malfunctions. The schedules entailed cycling the cells at different C-rates and started with a 12-hour constant voltage charge (CVC) to ensure the batteries were fully charged after varying storage times.

Some cells underwent meticulous testing under abusive conditions to intentionally push them to their functional limits, allowing for the analysis of strain and temperature responses under extreme stress. Detection of battery malfunctioning was always on the scope, but some cells were also cycled with the intention of discovering a correlation between strain and temperature evolution and the state of charge of the battery. Additionally, certain cycling schedules aimed to investigate battery degradation over numerous cycles by tracking changes in capacity and efficiency in relation to the observed strain on the cells.

This approach not only aimed to evaluate performance under normal operating conditions, but also to understand battery behavior under stress, and the FBG sensor's role in battery monitoring, contributing to safer and more efficient battery design.

### 3.5 FBG Calibration

As each FBG sensor exhibits varying sensitivity to both temperature and strain, it is crucial to individually calibrate each FBG utilized in the experiment to attain precise results. For this project, two optical fibers were used, one 2-FBG-array fiber and one single FBG fiber. Temperature calibration involves subjecting the FBGs to a controlled environment in a climate chamber alongside a thermistor. During the temperature calibration, the temperature was varied between 15°C and 35°C, matching the expected temperature range of the coin cell during the experiment. The setup of the calibration is displayed in appendix A together with the specifications of the FBGs.

Conversely, calibrating for strain sensitivity presents a more demanding challenge. High-

precision strain calibration can be achieved through the optical lever method, which measures small displacements optically [85]. Despite its significance, strain sensitivity calibration for the FBGs was not feasible for this project. As a result, strain sensitivity values were sourced from literature. They are typically around  $1.13 \mu\epsilon/pm$  [85], which is employed for this project.

An important aspect to consider when using the FBGs is that when the temperature chamber is operated at temperatures close to the room temperature (outside of the chamber), the temperature fluctuates. As the chamber turns the fan on and off to maintain the desired temperature, small fluctuations in the data are observed.

### 3.5.1 Calibration Results

Figure 3.3 depicts the reflected wavelength of each fiber Bragg grating. The different gratings were used to measure strain ( $\lambda_{B_\sigma}$ ), surface temperature ( $\lambda_{B_T}$ ) and surrounding temperature ( $\lambda_{B_{T_{ref}}}$ ). The figure shows a clear linearity between the wavelength shift of the strain grating and the chamber temperature. The reference temperature shows a slightly higher deviation from the chamber temperature, especially around 20-25 °C. This can be caused by the grating dangling in the air, making it susceptible to movements in the air.

The distinct temperature sensitivity for each grating is displayed together with the rest of the calibration results in table 2. The standard deviation and coefficient of determination,  $R^2$ , are obtained from the different data sets.

The  $R^2$  value is used to evaluate the strength of a model. It represents to which extent the variation of an independent variable contributes to the variation of a dependent variable [86]. In this case, the  $R^2$  shows how the correlation between the wavelength shift and temperature fits a linear regression model. As the values show, there is a close to linear relationship.

Both the standard deviation and the  $R^2$  value show that the reference temperature FBG deviates more from the temperature measurements. This strengthens the hypothesis of some irregularities, possibly from mechanical strain due to movement in the surrounding environment.

Table 2: FBG calibration results.

| Central Reflected Wavelength [nm] | Temperature Sensitivity, $K_T$ [pm/K] | Standard Deviation Error [pm/K] | $R^2$ value |
|-----------------------------------|---------------------------------------|---------------------------------|-------------|
| $\lambda_{B_{T_{ref}}} = 1530$    | 10.39                                 | 0.0127                          | 0.9975      |
| $\lambda_{B_T} = 1540$            | 8.96                                  | 0.0092                          | 0.9983      |
| $\lambda_{B_\sigma} = 1540$       | 9.16                                  | 0.0050                          | 0.9995      |

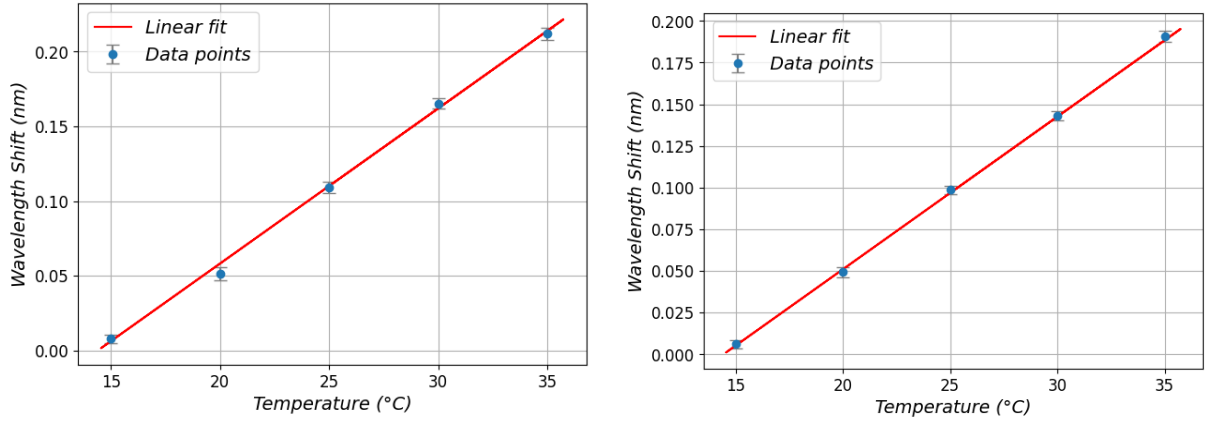
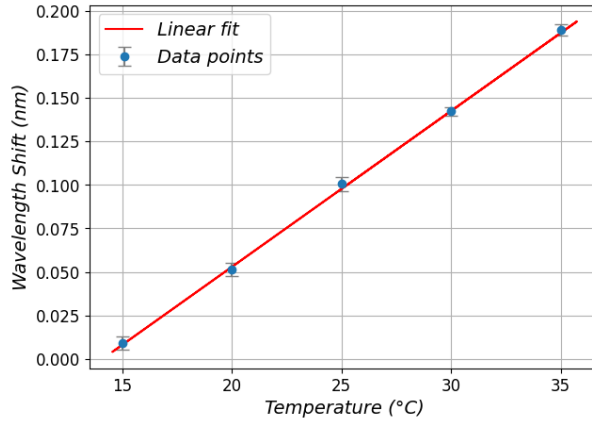
(a) Reference temperature calibration,  $\lambda_{B_{T_{ref}}}$ .(b) Temperature grating,  $\lambda_{B_T}$ .(c) Strain grating,  $\lambda_{B_\sigma}$ .

Figure 3.3: Results from FBG calibration.

### 3.6 Coin Cell Setup With FBGs

The coin cells were cycled with FBGs both during and after formation, to measure temperature and strain evolution. Some cells were also cycled with FBGs during formation. During cycling the coin cells were mounted on clips, exerting a compressive force on the cell surface. In retrospect, this likely affected the results. The experimental setup of the coin cell cycling with FBGs is shown in figure 3.4. There are two sensors fixed to the coin cell. The first sensor has two gratings, FBG 1 and FBG 2. FBG 1 is attached at both sides of the grating, intended to measure both temperature strain responses. FBG 2 is dangling over the edge of the coin cell and measures temperature changes inside the cabinet during cycling. Sensor two only has one grating, FBG 3. FBG 3 is attached at one side of the grating to only measure temperature changes on the surface of the coin cell and ideally avoid strain responses on the FBG.

Ideally, the temperature measured by FBG 3 is equal to the temperature affecting the wavelength shift of FBG 1. The setup intends that the wavelength from FBG 3 is only affected by temperature and no strain. By subtracting the surface temperature measured by FBG 3 from the interpreted wavelength of FBG 1, FBG 1 is then only left with the

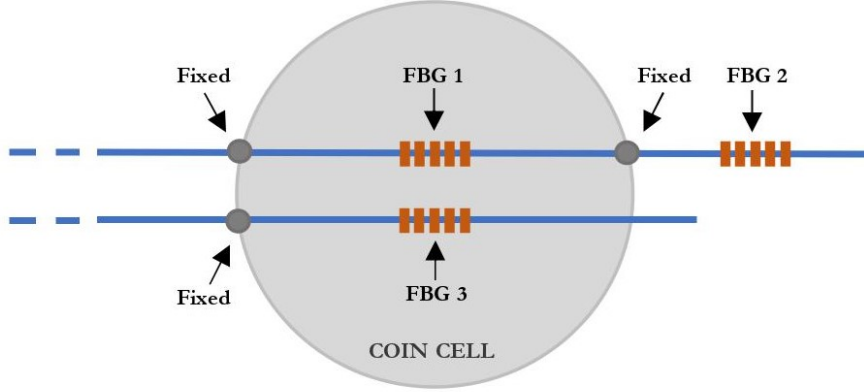


Figure 3.4: FBG setup for strain and temperature measurements on a coin cell.

strain response. Subtracting also the response measured from FBG 2 will accommodate for any temperature changes or fluctuations occurring inside the cabinet.

The complexity of the FBG setup is designed to allow for the solution of the unknown variables. The unknown variables include the temperature FBG 1 and 3 senses ( $T_1$ ) which is the combination of the battery surface temperature and the surrounding temperature, the surrounding temperature measured by FBG 2 ( $T_2$ ) and the battery external strain ( $\epsilon_1$ ):

$$\Delta\lambda_{FBG1} = K_{T,FBG1}\Delta T_1 + K_{\epsilon,FBG2}\Delta\epsilon_1 \quad (24)$$

$$\Delta\lambda_{FBG2} = K_{T,FBG2}\Delta T_2 \quad (25)$$

$$\Delta\lambda_{FBG3} = K_{T,FBG3}\Delta T_1 \quad (26)$$

Since FBG 1 and FBG 3 sense the same temperature ( $T_1$ ), including the battery surface and surrounding temperature, FBG 2 is used to simply subtract the surrounding temperature from these measurements. This makes it possible to both sense the battery surface temperature and the external strain of the battery, utilizing the reference sensor method. The reference sensor method is a well-established method used to isolate mechanical from thermal strain sensed by the FBG sensors. The method is described in Rao et al. [6].



### 3.7 Data Analysis

The data analysis for this project is comprehensive. It includes retrieving data from the Arbin system, Land system, and Enlight optic interrogator, as well as aligning, smoothing, and decoupling strain and temperature. All of which is done by coding in Python. Although much of the data is raw, smoothing functions have been applied particularly to the data from the FBGs to enhance the clarity of the presentation, focusing on removing trends likely attributed to background noise or effects from the reference fiber method.

## 4 Results and Discussion

This chapter presents the results of an investigation into the correlation between strain and temperature monitoring and the health situation of coin cells, mainly focusing on strain evolution. This study is based on the hypothesis that mechanical strain and temperature measurements can provide valuable insight into the degradation and overall health of LIBs. The experimental setup involved subjecting a series of coin cells to controlled charging and discharging cycles while continuously monitoring external mechanical strain and temperature using FBGs. The analysis focuses on identifying patterns and anomalies in strain behavior that could be directly correlated with the health of the cells. The results are intended to enhance the understanding of battery health indicators, potentially leading to more reliable and efficient BMSs. The findings are discussed in detail, supported by quantitative data and visual representations such as graphs and tables, to elucidate the relationship between observed mechanical strains and the health status of the coin cells. The results provided in this thesis are all based on the same types of coin cell batteries, as described in the method chapter.

### 4.1 Formation Cycles

Formation cycles at C/10 (0.1 mA) were conducted on all cells used in this study. Two of the coin cells were equipped with fixed FBGs during formation, as illustrated in figure 3.4. The results of these tests are presented in figures 4.1 and 4.2, which display changes in battery voltage, the applied current, and the corresponding strain changes. It is important

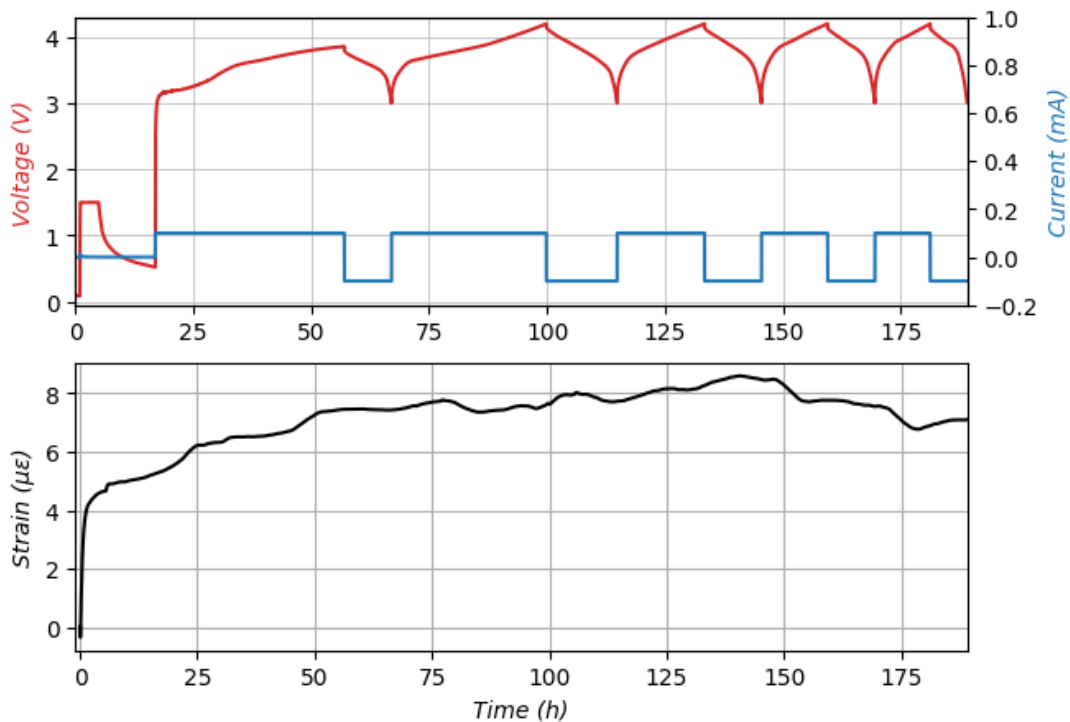


Figure 4.1: Formation cycles at C/10 for a NMC111/graphite coin cell with simultaneous strain measurements from FBGs.

to note that the strain depicted in figures 4.1 and 4.2 represents the overall strain build-up inside the battery over time. A smoothing function was applied to the data to mitigate background noise, likely caused by temperature fluctuations within the testing chamber. The temperature change from the coin cells was very small. Hence, these measurements were severely affected by background noise. The background noise is represented by small wave-like fluctuations on the strain curve, especially visible in figure 4.2 from about 100 hours until the end of the formation cycles. This shows that the strain measurements were hardly affected by the background noise. The temperature measurements from the coin cells are not included in the results, as the fluctuations were too prominent. Consequently, the focus is on the overall strain build-up throughout the formation cycles.

Both batteries follow an identical formation schedule with a two-hour rest before applying a small tap charge up to 1.5 V, then a CVC maintained for 4 hours. The current applied during this constant voltage phase is minimal and not visible in the graphs. Following the CVC, a 12-hour rest period is conducted for further electrolyte saturation. This initial phase is critical for stabilizing the electrode surfaces and enabling the electrolyte to begin penetrating the electrode pores [43]. During the rest, the voltage experiences a drop, nearly inversely proportional to time, indicating a relaxation of internal stresses and completion of the electrolyte's diffusion process.

The subsequent charging phase at a constant current of 0.1 mA (C/10) marks the beginning of active lithium intercalation, where the voltage steeply climbs to about 3 V and progresses slowly toward the cut-off at 4.2 V. However, neither battery reaches this

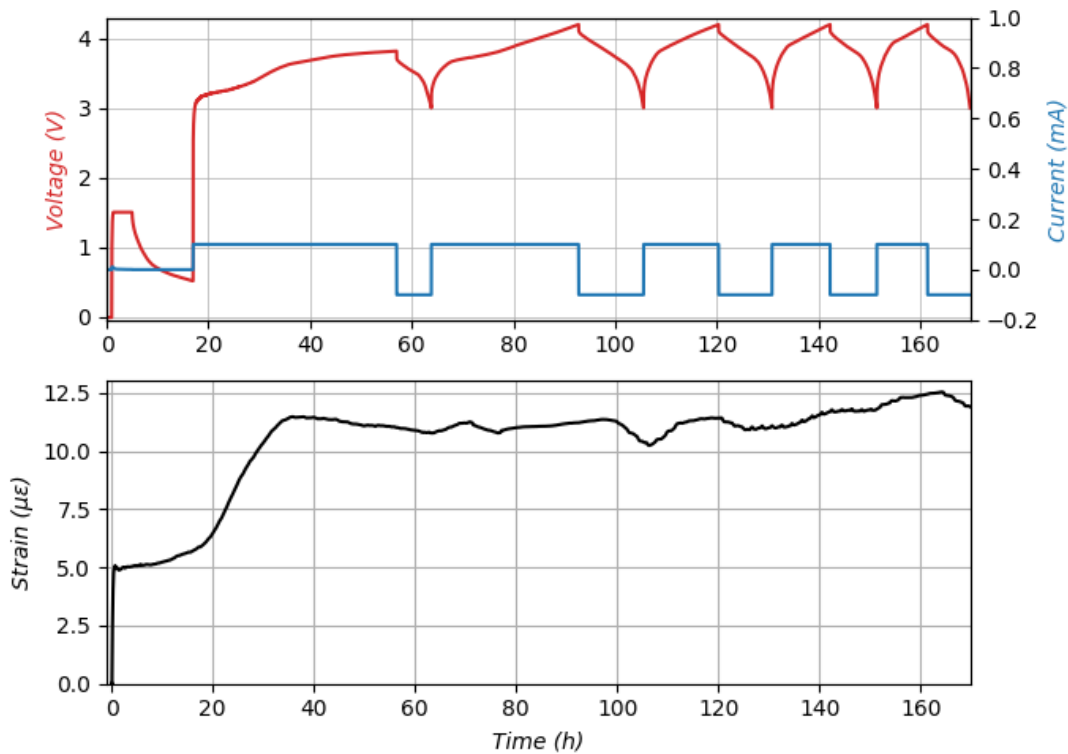


Figure 4.2: Formation cycles at C/10 for a NMC111/graphite coin cell with simultaneous strain measurements from FBGs.

threshold within the 20-hour limit, leading to a discharge down to 3 V before the next charging cycle begins. Notably, the discharge duration in figure 4.1 is slightly longer than that in figure 4.2, indicating a higher capacity in the former.

The final stages of the formation cycles show a decrease in duration. The last charge for the two batteries took about 11 and 10 hours, respectively, and discharges aligning at approximately 8 hours for both cells. Resulting in charge capacities of 1.1 mAh and 1.0 mAh, discharge capacities of about 8 mAh for both, and efficiencies of 73% and 80%, for the coin cells. This highlights the differences in electrochemical performance, which could stem from intrinsic variability in cell assembly or material behavior, as described in section 3.2.2.

Moreover, the strain responses in figures 4.1 and 4.2 show a steep increase initially, both of the same magnitude, about  $5 \mu\epsilon$ . This corresponds to the two-hour initial rest period before the tap charge is applied. Afterward, the corresponding strain increases gradually for both batteries towards the start of the first cycle. The cell in figure 4.1 displays a continual slow and gradual increase through most of the formation. However, the battery displayed in figure 4.2 shows a much steeper increase at the start of the first charge cycle, reaching almost  $12 \mu\epsilon$ , before stabilizing throughout the formation cycles, with only small variations.

The initial sharp strain increase during the first rest period can be a result of multiple factors. It might be a mechanical expansion of the casing. After the coin cells are assembled, they are crimped and pressed together, inducing stress in the material, which might cause the casing to expand a bit during the subsequent rest. Also, it can stem from electrolyte decomposition, which can generate gas [59]. However, this is not that likely before the activation of the cell. Furthermore, another source of this expansion can be swelling of the electrodes. During the rest period, the electrodes absorb the electrolyte, which can lead to expansion in the external casing [43].

Further expansion can be seen during the first initial tap charge for the battery in figure 4.1. This battery shows greater expansion when the tap charge is applied, but both cells exhibit some degree of expansion during the CC-CV tap charge. When current is applied, charge accumulates in the battery as the lithium ions start to intercalate. The intercalation can cause physical expansion of the electrode. However, the current applied is very low, decreasing from  $C/100$ , but sustaining a constant voltage over 4 hours results in a continuous insertion of lithium ions over an extended period. This likely causes some degree of expansion in the cells. Initial SEI layer formation can also contribute to strain increase, through mechanical stress caused by volume changes associated with the formation and growth of the layer [51].

As the formation cycles commence, the strain in figure 4.1 displays a slow and gradual increase, indicating steady mechanical stress accumulation within the battery structure throughout the cycles. This likely corresponds to a continuous uniform intercalation of lithium ions. In contrast, the battery in figure 4.2 shows a more abrupt strain increase to nearly  $12 \mu\epsilon$  at the onset of the first cycle, followed by a stabilization phase with

minor fluctuations. This variation might suggest differences in the mechanical stability or integrity of the electrode materials. This increase could correspond to one of the early lithium intercalation stages, together with the formation and growth of the SEI layer [17, 51]. As both batteries are inflicted by the same current, the differences in the continued strain increase possibly lie in discrepancies in the structural changes and SEI layer formation process occurring during the applied tap charge.

However, the deviations in both strain response and formation cycle efficiency could also arise from subtle differences in cell assembly. Variations could include slight differences in electrolyte volume, contamination levels, or minor electrode damage during manufacturing. These factors can critically influence both the mechanical and electrochemical dynamics inside the batteries.

## 4.2 Correlation Between Strain and Battery Degradation Through Long-Term Cycling

As previously mentioned in section 2.5, during the charge and discharge of a LIB, several unwanted side reactions may occur, leading to the gradual degradation of a battery. This degradation not only the battery's ability to retain charge but also its overall efficiency and lifespan. Further, battery aging effects may cause changes in volume behavior in LIBs, as suggested by Meyer et al. [10]. Consequently, the results presented herein offer an analysis of these degradation effects over an extended series of charge-discharge cycles, and if there is any correlation between the degradation of a battery and the strain measured by externally mounted FBGs. The temperature measurements did not provide any specific correlation throughout the cycling and were highly affected by background noise, and are therefore not included in the results.

Figure 4.3 displays the results from a battery that was cycled at a constant current charge at C/3 (0.3 mA) for 449 cycles between 3 and 4.2 V at room temperature (25°C) with FBGs attached to the surface. As the figure depicts, a clear trend can be viewed throughout these cycles, and coherence can be drawn between the battery efficiency, capacity, and strain built throughout the first 100 cycles. However, for the last 349 cycles, no clear correlation can be viewed other than a generally more flat trend. The low efficiency observed during the initial cycles matches with the increase in strain. This can be attributed to energy being absorbed by side reactions occurring within the cell. These side reactions, such as gas formation or extensive SEI formation, cause the battery to swell [8].

What should be mentioned is the capacity of the battery. The two batteries from the formation cycle in the previous section have capacities of around 1 mAh after formation. In contrast, the battery subjected to long-term cycling exhibited a significant reduction in capacity. Such capacity reduction is typical when batteries are cycled at higher C-rates, as stated by Peukert's law [37]. If the battery were cycled at a lower rate, such as C/10, it would likely maintain a higher capacity, similar to those observed in the formation cycles discussed in section 4.1. This behavior, known as capacity retention, is further elaborated

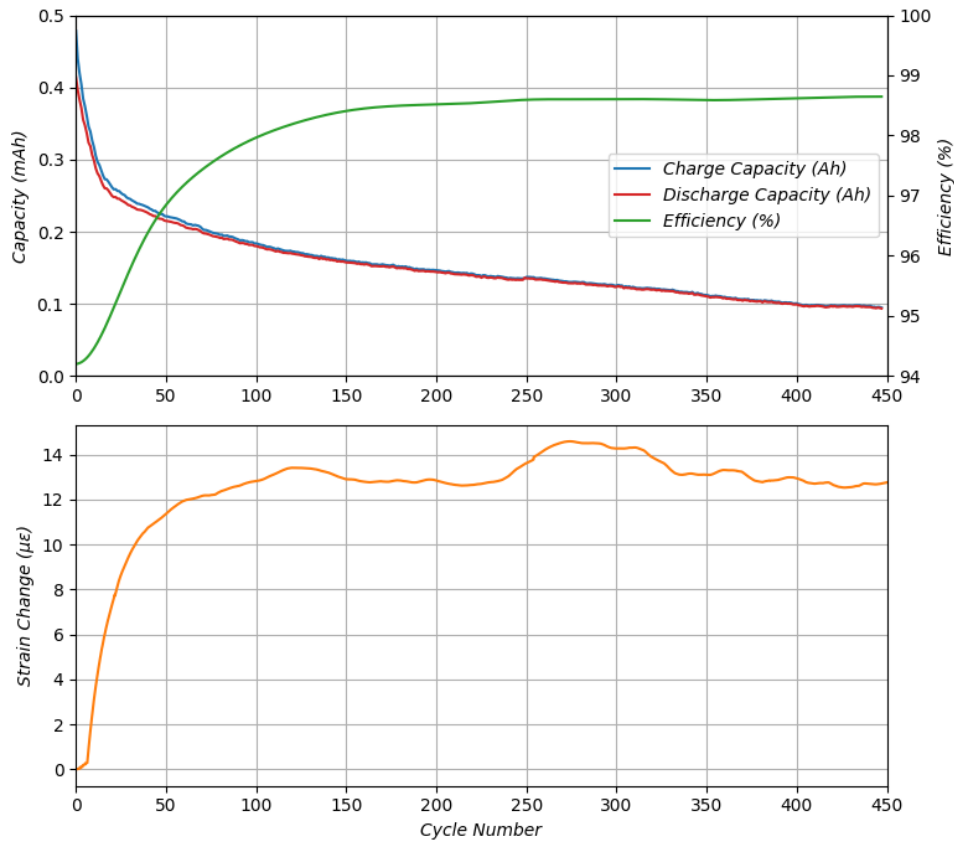


Figure 4.3: Battery cycled at  $C/3$  for 449 cycles.

in appendix A.

Moreover, there is a noticeable increase in strain during these initial cycles, which can be attributed to the mechanical adjustments of the battery materials, such as electrode expansion to accommodate intercalated lithium ions [17]. As the cycles progress beyond the first 100, both the charge and discharge capacities show a very slow decline, reflecting good cycling stability but also a gradual loss in capacity likely due to ongoing side reactions and material degradation, normal behavior for LIBs. The efficiency, calculated from equation 12, stabilizes throughout the cycles reaching close to 99%, indicating stable electrochemical processes despite the aging mechanisms in play. This is substantiated by the study performed by Yang et al. [21], where they found that a stable Coulombic efficiency curve correlates to a constant degradation rate, indicating stabilization within the cell. Additionally, the strain change exhibits only minor fluctuations, suggesting that the mechanical changes in the battery materials have reached a state of near-equilibrium after the initial adaptation phase.

This behavior suggests potential degradation mechanisms such as the growth of the SEI layer, which forms on the anode during the initial cycles and evolves further to consume lithium ions. Electrode material fatigue and side reactions such as gas formation or excessive SEI formation could also contribute to the observed capacity fade by consuming active materials and electrolytes, as well as potentially affecting the internal resistance and swelling of the battery.

### 4.3 Correlation Between FBG Measurements and Battery Malfunctioning

This chapter presents the results of an investigation into two coin cells. Both batteries had the same assembly technique and then went through the same formation at C/10 for five cycles. Further, the batteries were cycled with FBGs undergoing a CVC for 12 hours at 4.2 V to completely charge batteries. However, during this charge, one of the batteries showed a high strain increase at the end, probably caused by overcharging, which led to battery malfunctioning. Further investigation shows that the battery exhibited much lower capacity than the other batteries when cycled at C/3 after the 12-hour CVC, strengthening the hypothesis of battery malfunctioning. Consequently, this chapter further investigates strain and temperature as an indicator of battery malfunctioning.

It should be noted that several other batteries exhibited normal behavior. Showing similar results as the 'normal' battery.

#### 4.3.1 Using FBGs to Detect Battery Malfunctioning

The following subsection provides the results from a CVC, for the two coin cells. Both batteries had FBGs connected to them, as illustrated in figure 3.4. Figures 4.4 and 4.5 show the two different CVC cycles, with the voltage, current, and the corresponding strain measurements. Both batteries had a set voltage at 4.2 V for 12 hours after a two to three-week rest period, to ensure them being fully charged.

Both coin cells display similar voltage and current profiles. During the CVC, both cells maintain a consistent voltage level. The current exhibits a sharp decline at the onset of

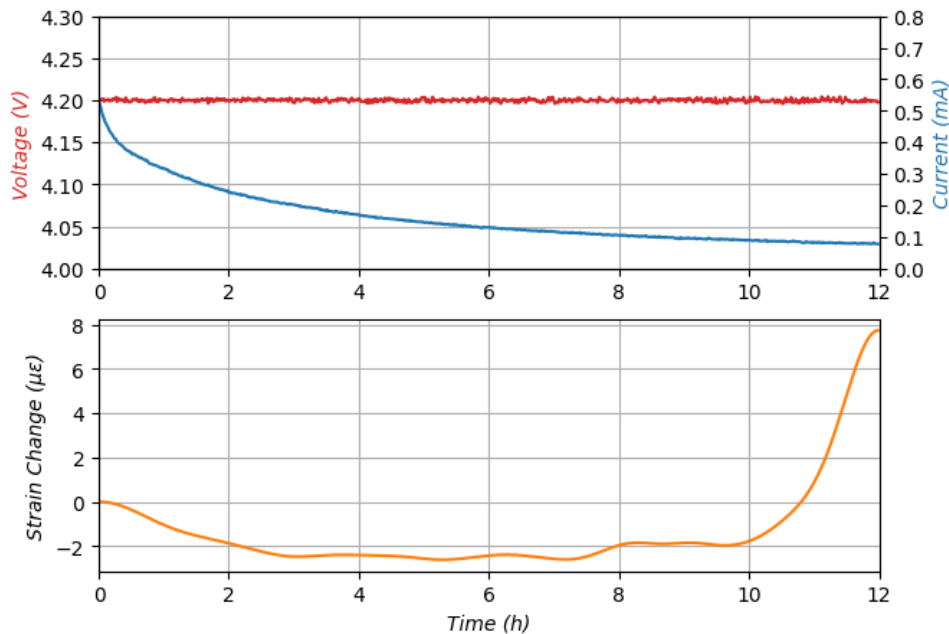


Figure 4.4: Strain change during constant voltage at 4.2 V and the corresponding voltage and current signals for the malfunctioning battery.

the CVC, which then levels off 4 to 6 hours into the charging process. Both coin cells ended the CVC after 12 hours with a very small current, indicating a fully charged state of the batteries.

However, the strain measurements are not that similar. The strain profiles can be related to mechanical changes in the cells, likely due to the expansion of the electrodes as lithium ions intercalate. For the normal battery, similarities can be drawn between the current and strain, as they are almost inversely proportional to each other. The moderate increase suggests a consistent and gradual intercalation process, without any abrupt changes.

The malfunctioning battery exhibits a small decrease in the strain profile at the start of the CVC before smoothing out. The strain shows a step increase at the end of the CVC, indicating a rapid change within the cell's structure, with a more substantial expansion. The magnitude of the strain increase is much greater than that observed in the other cell. This could be caused by substantial amounts of lithium intercalating abruptly due to sub-optimal SEI layer formation. Poor mechanical stability of the electrode material or gas formation within the cell could also contribute to this strain increase. Overcharging is likely the causative factor for this malfunction, as the steep strain increase occurs at the very end of the charging process.

Figure 4.6 and 4.7 show the strain and temperature profiles of the coin cells plotted against charge transfer, respectively. It is evident that the two batteries experienced different charge transfers during the 12-hour CVC, most likely due to their different states. The coin cells are made by hand in a laboratory, making them more susceptible to small variations due to personal deviation, as described in section 3.2.1. This can cause not only different capacities for each battery but also different self-discharge rates. Furthermore,

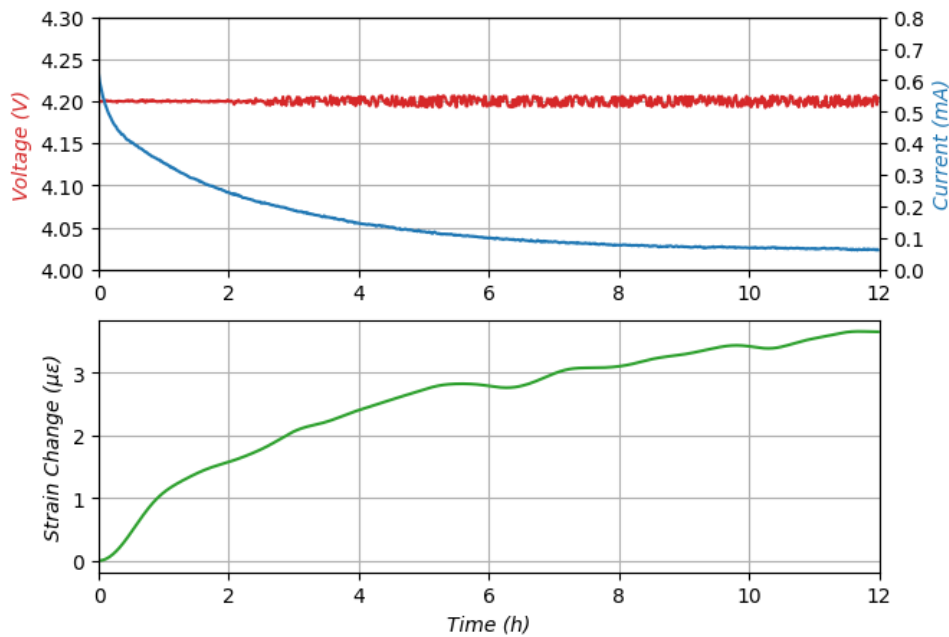


Figure 4.5: Strain change during constant voltage at 4.2 V and the corresponding voltage and current signals for the normal battery.



the batteries all had different rest periods after the initial formation cycles.

The relationship between strain changes and charge transfer that figure 4.6 depicts can provide a deeper understanding and indication of what is occurring inside the battery. Notably, the malfunctioning coin cell exhibits a sharp increase in strain towards the end of charging. This pronounced change, occurring with minimal charge transfer, suggests that side reactions, possibly involving gas production, are causing significant swelling of the battery.

In figure 4.7, the temperature trends reveal further insights into the electrochemical process occurring during charge storage. Both batteries show some degree of reduction in temperature throughout the CVC charge. However, the malfunctioning battery shows a substantially greater decrease in temperature than the other cells. Further, the temperature increases sharply towards the end of its charge cycle. This corresponds to where the strain increase occurs. A sharp temperature increase within coin cells is a typical sign of overcharging, also suggested and reported by Yang et al. [13]. Since it aligns well with the increasing strain measurements, it strengthens the hypothesis of battery overcharge. This thermal response, coupled with the observed strain, underscores the risks of side reactions that can compromise battery integrity and safety.

Analyzing the decrease in temperature measurements across the batteries, several factors come into consideration. One plausible explanation is the relationship between gas formation and thermal conductivity. When internal gas formation occurs, as suggested by the increase in strain, it generally results in diminished heat conductivity from the battery core to its surface. This phenomenon, likely impacting the normal battery, could explain the observed temperature reductions in this cell.

In contrast, the malfunctioning battery exhibits a slight decrease in strain alongside decreasing temperature. A substantial gas production within the cell could substantiate the temperature decrease seen in 4.7, as gas within the cell could lower the thermal con-

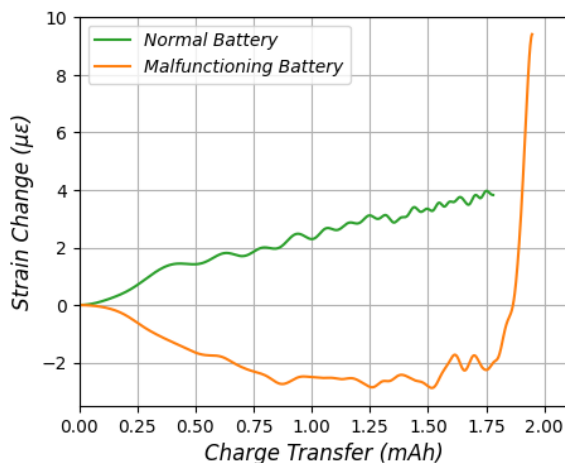


Figure 4.6: Strain change vs. charge transfer for the normal and malfunctioning battery.

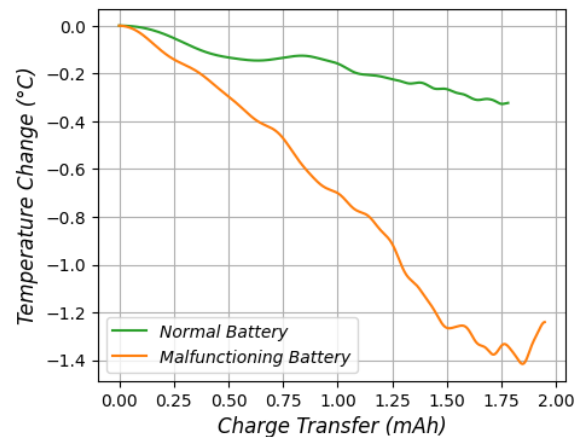


Figure 4.7: Temperature change vs. charge transfer for the normal and malfunctioning battery.

ductivity, which in turn could cause further unwanted side reactions resulting in an even higher strain increase. However, since the strain is also decreasing, this does not suggest any gas formation inside the cell before the sharp increase at the end. Since the shape of the decreasing temperature and strain is very similar, it can be an indication of experimental errors or anomalies, such as inaccuracies in reference temperature measurements. Potential sources of such errors could include variations in the ambient temperature of the testing chamber or other experimental setup issues. Given these considerations, the observed changes in temperature and strain for this cell should be approached with caution, and it may be premature to draw definitive conclusions from this data alone.

Therefore, while the decrease in temperature in the normal cell could be attributed to reduced thermal conductivity due to gas formation, the results from the malfunctioning cell necessitate a more cautious interpretation. Possible experimental errors must be taken into account. This would involve reviewing the experimental setup, re-calibrating sensors if necessary, and considering the influence of environmental factors on the measurement results. Such steps could help clarify whether the observed phenomena are intrinsic to the battery's behavior or are artifacts of the experimental conditions.

After the CVC all the batteries were cycled at C/3 between 3 and 4.2 V. The result from this is presented in table 3. The malfunctioning battery had a much lower charge and discharge capacity than the normal battery. This reduction in capacity is a strong indication of a malfunctioning coin cell, strengthening the hypotheses regarding its loss in performance.

Further analysis revealed a notable increase in strain within the malfunctioning battery, with measurements showing a steep rise to  $60 \mu\epsilon$ . This increase in strain is indicative of internal side reactions possibly involving gas generation. Such side reactions could arise from the decomposition of electrolyte materials or other internal chemical processes that typically produce gases, leading to the expansion of internal components and the observed strain.

The combination of lower electrochemical capacities and elevated strain measurements provides substantial evidence that the coin cell is malfunctioning. This, coupled with the anomalies observed during formation cycling (elaborated later in section 4.3.2), suggests internal degradation mechanisms that not only impair the battery's capacity but also pose potential safety risks. The presence of gases within the cell may lead to increased internal pressures, potentially compromising the structural integrity of the battery and leading to risks of thermal runaway. Additionally, it does not make sense that a battery can have higher than 100% efficiency, as displayed in table 3. However, this may indicate that the battery overcharged, during the 12-hour CVC. An overcharge can lead to some form of structural degradation. Hence, it can be that the battery is not accepting charge that well.

Additionally, structural changes in the electrode material due to lithium intercalation could also have some effect on the expansion. The distinct strain evolution recorded during battery cycling underscores the effectiveness of FBG sensors in real-time health

Table 3: Mean charge and discharge capacity and corresponding efficiency and strain change during 4 cycles at C/3 after CVC for the coin cells.

|                                 | Normal Battery | Malfunctioning Battery |
|---------------------------------|----------------|------------------------|
| Charge Capacity [mAh]           | 0.518          | 0.077                  |
| Discharge Capacity [mAh]        | 0.498          | 0.094                  |
| Efficiency                      | 96.1%          | 122%                   |
| Strain Change [ $\mu\epsilon$ ] | 2.2            | 60.2                   |

monitoring and failure prediction for lithium-ion batteries. By correlating specific strain patterns with comprehensive electrochemical and thermal data, FBG sensors can offer a promising approach for enhancing battery safety and operational efficiency, as concluded by Meyer et al. [10]. Further, Meyer et al. also suggested that monitoring external strain is more effective in capturing early indicators of battery failure than temperature monitoring, which the results from these experiments underscore. Cui et al. [12] also suggested that strain can be used as an indicator for gas formation, which again is an early indicator of battery failure and possible thermal runaway, underscoring these findings.

However, it is important to differentiate that not all observed strain increases represent negative battery behavior. The initial strain increase seen during formation in several cells correlates with chemical activation during the early stages of charging. This reflects normal and expected behavior associated with the initial intercalation processes where electrodes expand. This highlights that strain increases at the start of charging do not necessarily indicate a malfunction but rather are indicators of chemical activation within the battery. This understanding of strain behavior, enabled by FBG sensing, is crucial for implementing effective monitoring systems that enhance both the safety and efficiency of battery technologies.

### 4.3.2 Formation Cycles

The following analysis presents the data from the formation cycling of the healthy and malfunctioning batteries discussed in section 4.3.1. The formation cycles provide the basis for further cycling, laying the foundation for efficient and stable cycling. Discrepancies in the initial cycling might indicate later malfunctioning, underscoring the hypothesis of section 4.3.1, that the FBGs monitored early indication of battery malfunctioning.

Figure 4.8 shows the whole formation cycling of the malfunctioning cell. The 20-hour cut-off was not applied to this battery, nor the normal one. The curve in figure 4.8 shows an abnormal voltage response in the beginning compared to a normal formation cycling, as seen in figures 4.1 and 4.2. During the CC phase of the tap charge, the malfunctioning cell fails to reach 1.5 V, only going up to 0.045 V. During the CV phase, it fluctuates around 0.05 V. The voltage then decreases to zero during the 12-hour rest and drops slightly below zero at the end of the rest.

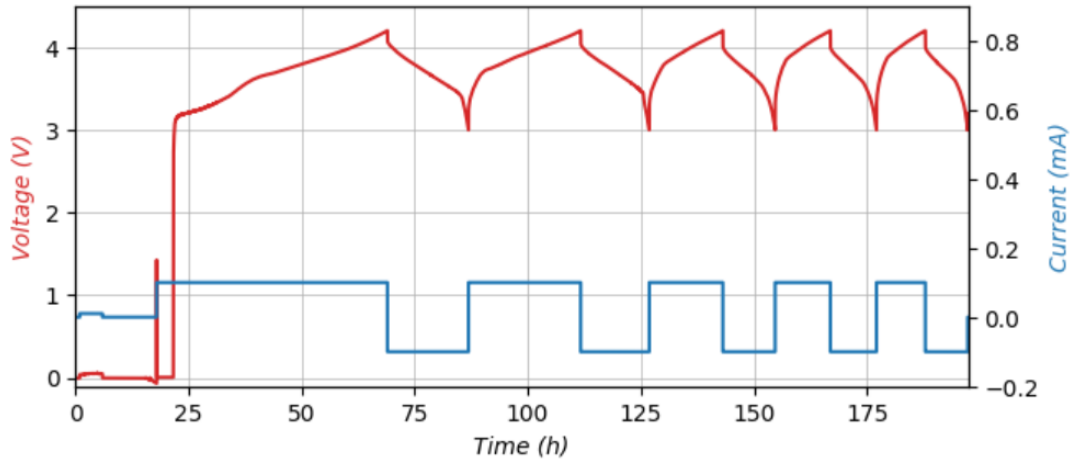


Figure 4.8: Voltage and current profile vs. time for the formation cycling of the malfunctioning coin cell.

The normal coin cell, however, initially shows a rapid increase in voltage as it begins to charge until around 3 V, indicating that the cell is accepting charge efficiently. Further, a steady increase in voltage and capacity is observed, until the charge is cut off at 4.2 V. This plateau from 3 to 4.2 V is typical in NMC111/graphite batteries, and represents the phase where the chemistry stabilizes.

The distinctly different behavior of the malfunctioning cell is mainly attributed to the voltage dropping to close to zero after a short initial charge. The sudden voltage drop could indicate a failure or defect in the cell, as the initial charge fails. This could be due to a breach in the cell's integrity, which could interrupt the charging process.

The tap charge, meant to prevent corrosion, failed to reach a sufficient voltage level. Undesired side reactions may have occurred inside the battery due to this fault during formation. This irregular behavior might be caused by a minor occurrence during the assembly process, as discussed in section 3.2.1.

The charge and discharge capacity of both coin cells decrease considerably over the five formation cycles, as shown in figure 4.9. The capacity profile of the cells can be used to assess the reversibility, as the difference of the charge and discharge capacity represents the Coulombic efficiency [22]. Irreversible reactions occurring in the cells can be observed from the decrease in capacity throughout the cycles.

The malfunctioning cell shows abnormal behavior at the beginning of the charge in cycle one, and reaches the lowest capacity of 5.13 mAh after the first charge. The normal coin cell reached a capacity of 6.34 mAh after the first charge, 19% higher, although this evened out throughout the five formation cycles.

There is a significant drop in capacity for both cells from the first to the second cycle, which is typical during formation. This drop is commonly caused by irreversible reactions occurring during the first cycle, such as the formation of the SEI layer [51]. From the second cycle and onward, the cells appear to stabilize, with a steady reduction in

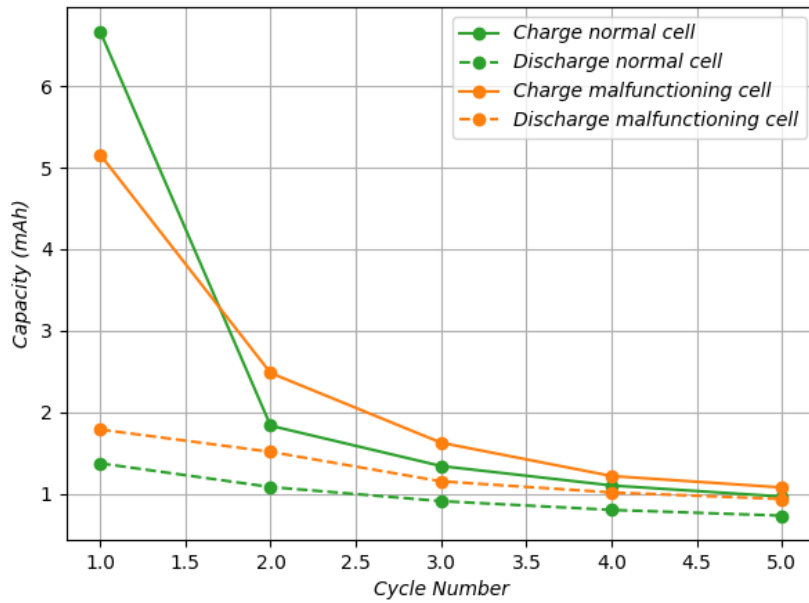


Figure 4.9: Charge and discharge capacity over the first five cycles during formation for the normal and malfunctioning coin cells.

capacities. The cells are behaving more predictably, indicating that the major irreversible changes occurred during the first cycle. The subsequent cycles reflect more of the actual capacity of the cells. Both cells have roughly equivalent charge and discharge capacities after formation.

The discharge capacities are consistently lower than the charge capacities for all cycles. This is typical and it reflects the efficiency of the cells, which commonly increase during cycling. The substantial difference between the charge and discharge capacity in the first cycle can be attributed to the great consumption of lithium ions used to form the SEI layer [42]. Other irreversible reactions can occur during the first charge, consuming more electrolyte or active material, and reducing the available charge amount for discharge. Also, not all lithium ions can de-intercalate from the anode due to the discrepancy in the actual and reversible capacity of the electrodes [25]. This results in a higher apparent capacity during the initial charge that cannot be matched during the first discharge.

Further into the cycling, the electrolyte has had more time to fully saturate the active material, improving the ion transport and reducing internal resistance. This can enhance the capacity. During the first charge, some lithium ions may become trapped in less accessible parts of the electrode or consumed in side reactions. This makes them inactive for the first discharge. Some of these ions can be reactivated allowing them to participate in the subsequent charge. An effective SEI layer formation can also contribute to better utilization of the battery capacity.

Figure 4.10 shows the differential capacity plotted against voltage for the first charge cycle of the normal and malfunctioning batteries. The plot provides insight into the

electrochemical processes occurring within the cells at different voltage levels. The size of the peaks represents the capacity contribution of specific chemical reactions. Differential capacity analysis is a commonly used method to investigate degradation mechanisms and estimate the SoH of batteries. Observing changes in the differential capacity throughout the cycling can be used to provide insights into the future behavior of the cell.

The peaks in the plot indicate specific reactions where a substantial amount of lithium ions are intercalated in the graphite material, where figure 4.10 suggests a generally high activity involving lithium intercalation for the normal coin cell. Lithium forms various stages of lithium-graphite intercalation compounds ( $C_6 \rightarrow Li_xC$ ) during cycling, where  $x$  varies during the different stages [17].

The curve of the normal cell starts with a gradual increase, leading up to a series of peaks in the voltage range of 3.15 to 3.4 V. This likely corresponds to the initial stage of intercalation and formation of the SEI layer. The malfunctioning cell follows the same development, with a slight delay.

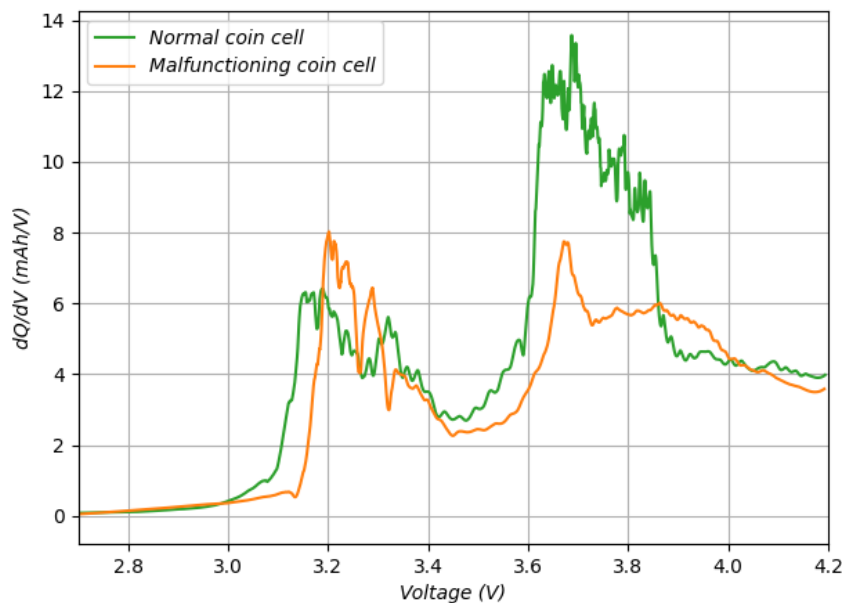


Figure 4.10: Differential capacity plot for the first charge cycle for the normal and malfunctioning coin cells.

The voltage range from 3.4 to 3.6 V is dominated by small fluctuations and less pronounced peaks, for both cells. This represents the continuous intercalation of lithium into the graphite structure, where the arrangement of lithium ions within the graphite layer changes. The steep increase at 3.6 V for the normal cell might be associated with a phase transition. The same peak occurs at 3.7 V for the malfunctioning cell, just of a lower magnitude. This represents less lithium intercalated for this cell.

Further, from 3.6 to 3.85 V a dense range of multiple sharp peaks is observed for the normal cell. The concentration of these peaks suggests a very active phase of lithium

intercalation, resulting in a rapid and efficient uptake of lithium ions in the graphite electrode. These peaks might represent higher stages of lithium intercalation. It could also indicate structural rearrangements, as the graphite lattice adjusts to the high concentration of intercalated lithium [17].

Moreover, from 3.85 V until 4.2 V, a steady decrease in differential capacity is observed for both cells. This suggests that the electrochemical reactions are stabilizing and that the majority of the accessible lithium is intercalated. Allover, the malfunctioning cell, which showed abnormal behavior during the tap charge and first charge cycle, displays a somewhat similar curve to the normal cell, however less activity is observed.

Figure 4.11 shows the differential capacity during the first discharge cycle of the same two cells, representing the de-intercalation of lithium ions. A rapid decrease from 4.2 to 3.9 V can be observed for both cells, indicating a substantial amount of lithium released from the graphite. Further de-intercalation occurs in both cells, where the malfunctioning cell all over shows a more active de-intercalation process.

The normal coin cell shows a relatively smooth curve, representing a stable and continuous de-intercalation of lithium ions. However, the magnitude is much lower than the other battery, suggesting less lithium being transferred back to the cathode.

The malfunctioning cell shows a more fluctuating curve, indicating a less uniform de-intercalation process possibly due to varying resistance in the cell. These sharper peaks might indicate that the cell undergoes more abrupt changes in the electrochemical state, where irregularities in the electrode structure or local variations in the SEI layer could affect how the lithium exists in the graphite. Li et al. [54] observed expansion, wrinkles,

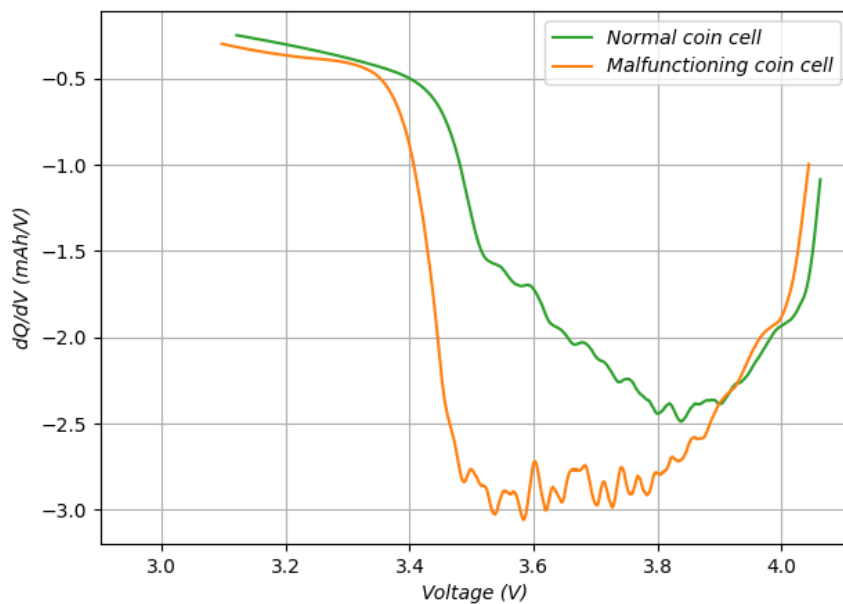


Figure 4.11: Differential capacity plot for the first discharge cycle for the normal and malfunctioning coin cells.

and cracks in the graphite layers caused by surface polarization, which could be the cause of the irregularities observed. However, they report this non-equilibrium behavior to be most prominent at high charging rates, which is not the case during formation. These peaks observed could also just correspond to the reverse process of specific intercalation stages, especially the stages where lithium was densely packed such as the transition from  $LiC_6$  to  $LiC_{12}$  [17].

Figure 4.12 shows the differential capacity for the second charge of the normal and malfunctioning coin cells. This plot gives insight into the stabilization of the cells after the initial cycle. During the first cycle a stable SEI layer is normally formed and the major part of lithium consumption has already occurred [42]. Also, defects in the graphite structure can disappear over several de-/intercalation cycles, as observed in a study by White et al. [55]. Consequently, the differential plot of the second cycle is normally smoother, such as the curve for the normal battery depicts. However, the battery which later malfunctioned still shows an unstable intercalation process. This suggests a more reactive or less uniform structure of the battery's graphite electrode.

Overall, the analysis of the formation cycle of the two cells reveals some differences possibly indicating abnormal behavior of the malfunctioning cell. This cell showed irregularities during tap charge and failed to fully charge at the first attempt during the first cycle, displaying a sudden voltage drop. This could indicate internal faults in the cell, resulting in later malfunction. The differential capacity plots showed that the normal cell stabilized after the first charge, whereas the malfunctioning cell displayed more unstable behavior. This may indicate structural irregularities within the malfunctioning battery, strengthening the hypothesis represented in section 4.3.1, that the strain increase measured by the

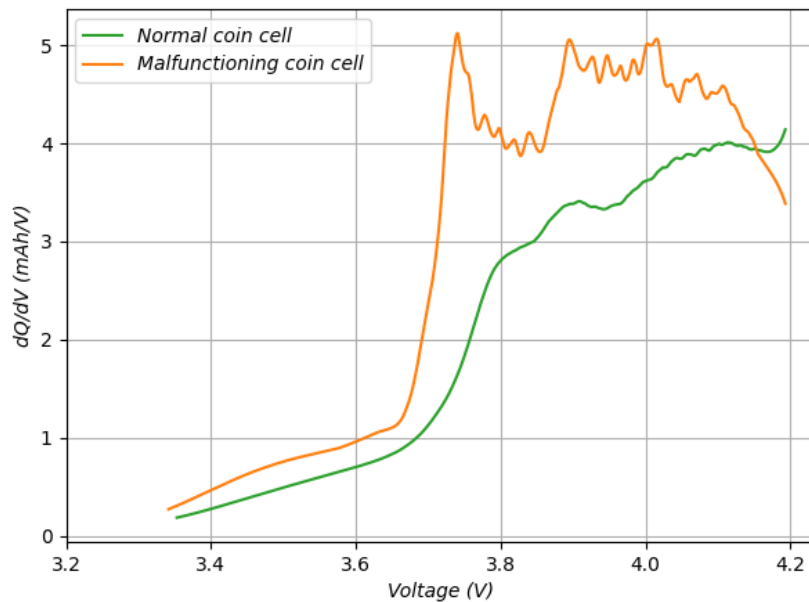


Figure 4.12: Differential capacity plot for the second charge cycle for the normal and malfunctioning coin cells.



FBGs can be interpreted as an early indicator of battery failure.

## 4.4 Detecting Battery Malfunctioning Under Abusive Conditions

In this analysis, the results from an experiment conducted under abusive conditions on three new coin cells are presented. Each battery was subjected to a constant voltage of 3 V with the explicit aim of depleting the batteries and thus inducing potential failure modes by destroying the electrode structures. Data was collected and plotted for current, voltage, strain change, and temperature change to analyze the battery response under these harsh conditions. All experiments were aborted due to safety mechanisms in the Arbin system, which indicated battery failure.

### 4.4.1 Coin Cell X

Figure 4.13 presents the evolution of coin cell X, which cycles up to 3.5 hours before the Arbin system aborted the test. Initially, the voltage fluctuates around  $3\text{ V} \pm 0.4\text{ V}$ . Concurrently, the current is very high, before dropping to a negative current, suggesting a discharge of the battery. This continues to approximately the 2-hour mark, after which the voltage seems to stabilize. After 2.5 hours, the current increases to a positive current of around 15 mA. However, the voltage does not seem to be affected by this current profile before 2.8 hours. Further, the voltage shows significant fluctuation until the safety stop. This may be a reflection of low available charge due to battery degradation under abusive conditions.

Looking at the strain and temperature evolution of coin cell X, both parameters exhibit similar characteristics: a steep initial increase followed by a more gradual rise until the

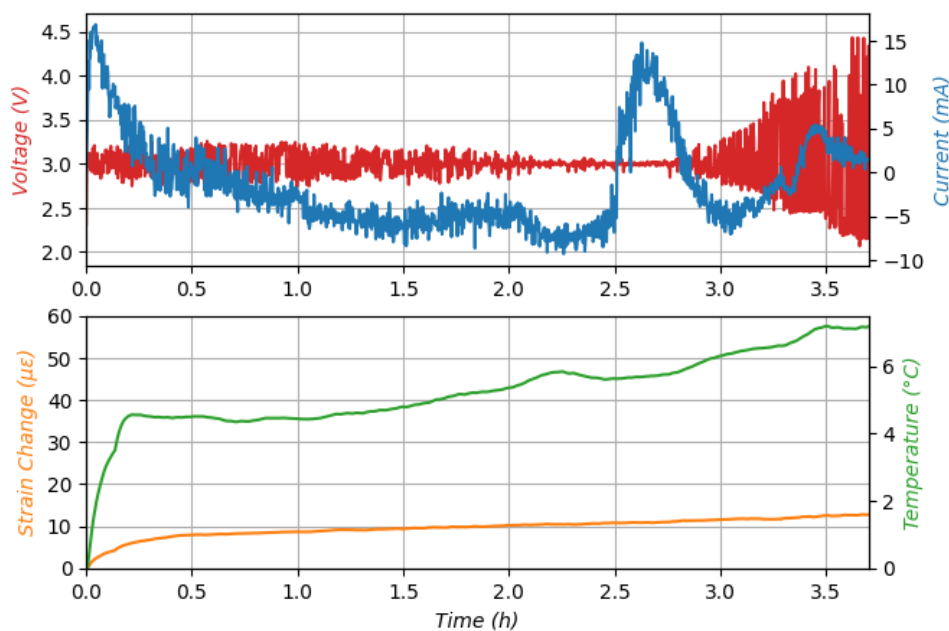


Figure 4.13: Strain and temperature signals during CV at 3 V, along with the corresponding voltage and current signals for coin cell X.

end. It is worth noting that the initial strain increase is of the same magnitude as that observed in the malfunctioning battery discussed in the previous section (section 4.3.1), around  $10 \mu\epsilon$ . This may serve as an early indicator of battery malfunction.

Additionally, the temperature also experiences a step increase during this initial phase. Compared to the previous section, the malfunctioning battery showed an increase in temperature coinciding with the strain increase. Furthermore, experiments conducted by Yang et al. [13] demonstrate a similar temperature response during the overcharge of a battery, characterized by a steep temperature increase.

One possible reason for the high initial temperature rise could be the magnitude of the current. High current can lead to increased ohmic losses, which dissipate as heat, thus contributing to the temperature rise. Further, since the temperature increase is so high, the strain might come from thermal expansion in the material, rather than increased internal pressure from sources such as gas formation. Consequently, the strain increase might not be indicating typical battery malfunction. Hence, this result underlines the importance of dual-parameter sensing.

#### 4.4.2 Coin Cell Y

Figure 4.14 displays the results of coin cell Y. In this scenario, both the voltage and current display notable instability, of a similar magnitude as coin cell X. The short period of the CV before safety abortion strengthens the hypothesis of malfunction within the cell. The rapid rise in strain and temperature further underscores susceptibility to mechanical and thermal degradation under harsh conditions. The magnitude of the strain increase is significant, around five times what is seen for coin cell X. This indicates severe mechanical

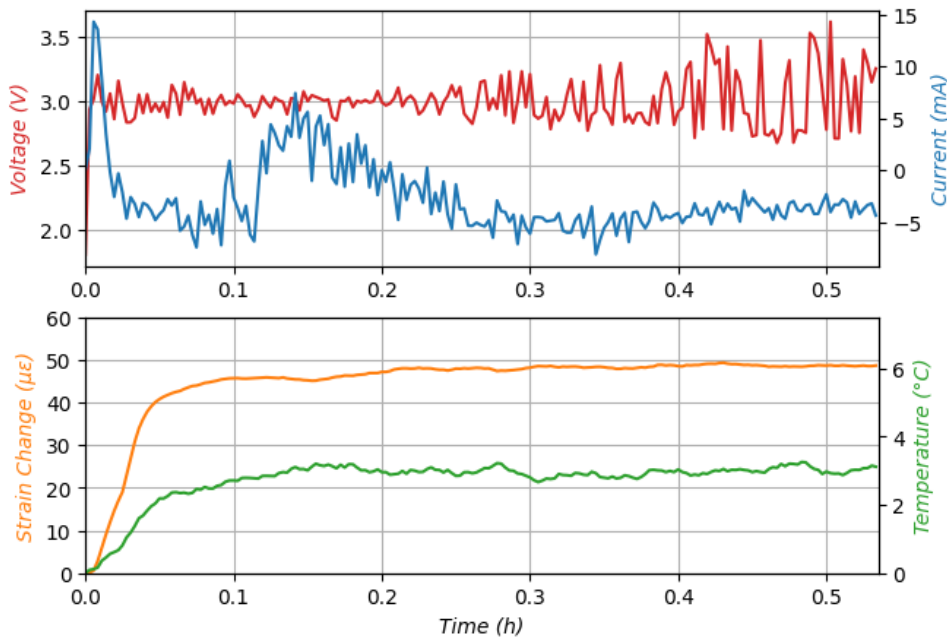


Figure 4.14: Strain and temperature signals during CV at 3 V, along with the corresponding voltage and current signals for coin cell Y.

stress within the cell, possibly from gas formation. Additionally, since the temperature increase is much lower than that of coin cell X, the main strain increase does not likely come as a reason of thermal stress in the material. However, some thermal stress might occur since the temperature increases.

#### 4.4.3 Coin Cell Z

Coin cell Z, depicted in figure 4.15, reveals a higher voltage variation than the two other cells, increasing throughout the cycling. This cell also exhibits a very short CV cycling before the safety mechanisms of the system abort the test. The current applied is significantly lower than the other cells, possibly indicating a more reactive or fragile battery state. Notably, the strain registers an early sharp rise, which is even higher than coin cell Y and temperature increases steadily, signaling an accelerated rate of degradation, likely leading to faster failure.

Upon reviewing the raw data, it becomes evident that the fluctuations in current are more substantial than what is depicted in figures 4.13, 4.14, and 4.15. This observation is substantiated by the charge and discharge capacities, which both increased at each 10-second logging interval. These variations underscore the intense and dynamic internal reactions within the battery, indicating a more volatile response to the testing conditions than initially suggested by the graphical representations of current and voltage. This provides a clearer picture of the battery's critical state under the abusive testing conditions.

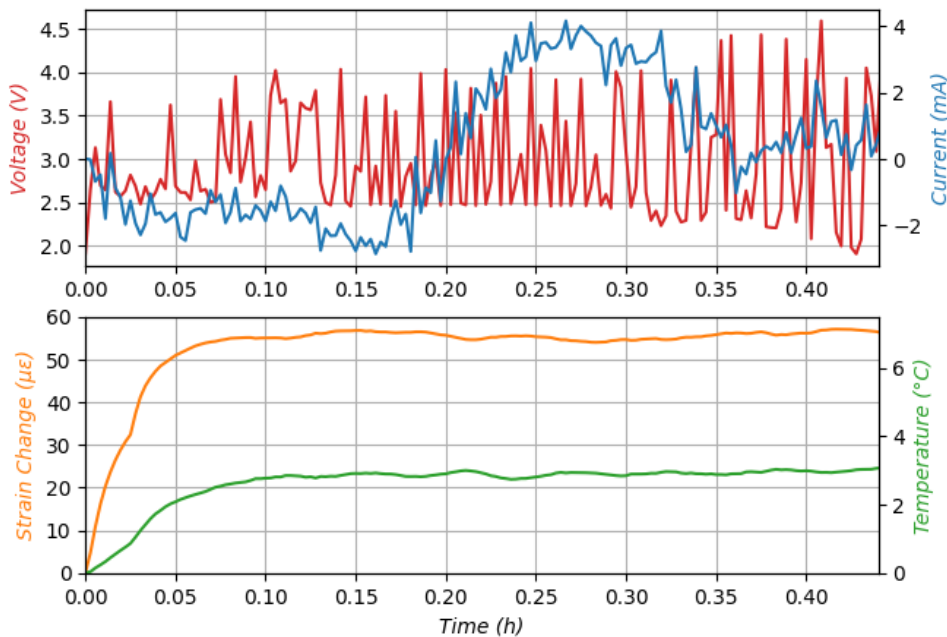


Figure 4.15: Strain and temperature signals during CV at 3 V, along with the corresponding voltage and current signals for coin cell Z.

#### 4.4.4 Strain and Temperature Behaviour vs. Charge Transfer

The strain and temperature rise for the three coin cells over the span of charge transfer is displayed in figures 4.16 and 4.17. Firstly, figure 4.16 shows that the main strain increase occurs over a small charge, similar to that of the malfunctioning battery in figure 4.6. Further, the same trend can be seen for the temperature in figure 4.17, indicating there is a correlation between battery behavior and the evolution of strain and temperature.

The magnitude of strain increase in coin cells Y and Z is significantly higher than in coin cell X. Coin cells Y and Z exhibit a strain magnitude similar to that of the malfunctioning battery described in section 4.3.1 during cycling at C/3, around  $60 \mu\epsilon$ . This, coupled with the much shorter cycling time before the Arbin system shut down the experiment, suggests high internal pressure due to gas formation. This could in the worst case lead to thermal runaway, as suggested by Cui et al. [12].

To conclude the findings of these experiments, externally mounted FBGs are effective in detecting battery swelling, likely caused by gas formation or thermal expansion in the coin cells, which can serve as an early indicator of battery malfunction and potential thermal runaway [10]. The gas formation results in significant strain increase and, when combined with temperature rises, provides critical insights into the battery's internal state. These indicators can be used to predict and prevent failures such as thermal runaway. Further supporting this hypothesis is the observation that the Arbin system takes longer to abort experiments than the time it takes for strain increases to occur. Therefore, integrating FBGs for strain and temperature monitoring is a valuable tool for battery safety. The results highlight the importance of continuous strain and temperature monitoring as part of a comprehensive battery management system to ensure safety and reliability under various operating conditions.

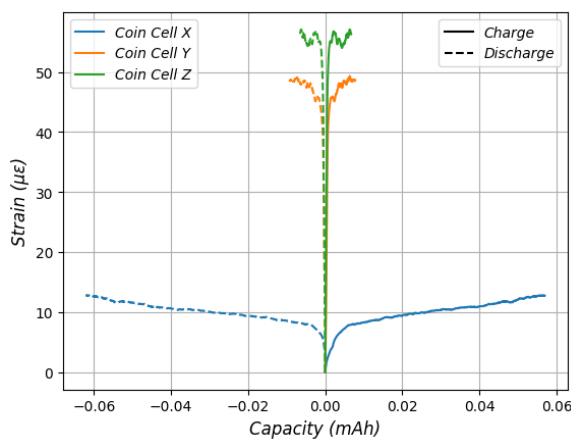


Figure 4.16: Strain change vs. charge transfer for the three coin cells.

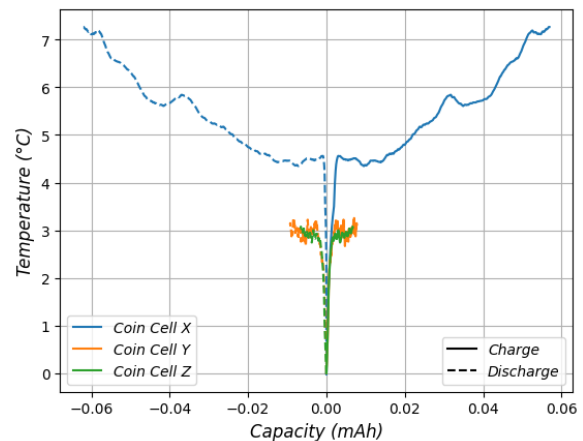


Figure 4.17: Temperature vs. charge transfer for the three coin cells.

## 4.5 Relationship Between Strain and SoC

During this study, several experiments have been conducted with FBGs fixed externally to coin cells. Different cycling schedules were carried out, but no relationship between

the strain response and the SoC and DoD has been found for this particular setup. There are several sources of errors that could account for this.

Firstly, the coin cells have a hard casing which makes it difficult to measure the strain on the surface. A soft casing would more easily exhibit deformation on the surface, giving a better response to the fibers. Most previous studies on FBG sensing with batteries utilize pouch cells, as they have a flexible casing. For studies performed on cylindrical or prismatic cells, where FBG sensors have been utilized, the primary focus is commonly on temperature monitoring rather than strain.

Internal strain and temperature measurements could increase sensitivity and overcome the issues associated with hard casings. A more direct measurement is possible, with precise reflection of the internal state of the cell. However, embedding the FBG into the cell is an invasive procedure that might impact cell performance, by altering electrochemical properties or physical integrity. For in-situ measurements, external sensing is the most practical solution, as the fiber is accessible and easy to install. Nevertheless, these sensors are susceptible to external environmental factors. In this study, variations in the environment within cycling cabinets demonstrated how external conditions could influence the reliability of the data collected by externally mounted fibers. Depending on electrode material and casing, as well as the objective, both internal and external measurements could give sufficient results.

The coin cells also have relatively small electrodes. Small electrodes mean smaller amounts of lithium participating in reactions and intercalating in the electrodes, resulting in less overall expansion. For the same reason as the electrode size affects strain response, the size of the cell is of significance. Since the strain and temperature generated are relative to the cell area, performing experiments on a bigger cell would likely increase both absolute values.

The background noise occurring with this specific set-up has turned out to be substantial. The small strain variations cannot be detected through the hard casing, as the magnitude of the noise significantly impacts the measurements. Additionally, the batteries were mounted using clips that applied pressure from both sides of the cells. This constant pressure counteracts the volumetric expansion of the cell, which limits the strain signals that can be detected. Implementing more loosely attached terminals could potentially enhance the sensitivity and increase the response of the FBG sensors, allowing for more accurate strain measurements.

The electrode material also plays a role in the strain evolution as the volume expansion varies greatly. The typical volume variation of graphite anodes during lithiation and delithiation is about 10%. However, other anode materials such as those composed of silicon may be favorable for external FBG sensing, as suggested by Wahl et al. [73].

The primary challenges in estimating SoC through FBG measurements in this setup include the small size of the battery, its hard casing, and the compressive force exerted by mounting clips. Regardless, the experimental setup is satisfactory for detecting malfunctioning batteries.

---

## 5 Conclusion

In this work, fiber Bragg gratings (FBGs) were successfully mounted on NMC111/graphite coin cells for real-time strain and temperature measurements, critical parameters for monitoring the state of lithium-ion batteries. The coin cells were self-assembled in a controlled environment, ensuring minimal contamination and consistent performance. FBGs were calibrated in a climate chamber using a thermistor, demonstrating a linear relationship between the reflected Bragg wavelength and temperature. This calibration confirmed the accuracy and reliability of FBGs in measuring temperature changes on the coin cells, enhancing the precision of strain and temperature monitoring during battery operation.

During the experiments, FBGs were externally mounted on coin cells to monitor the strain and temperature evolution of lithium-ion batteries during formation, normal cycling, aging, and under abusive conditions. The correlation between strain and battery state parameters such as SoC and SoH was explored. However, no direct relationship was found in this setup, likely due to the small variations within a single, small cell and the hard casing of the coin cells. Nevertheless, a correlation between strain increase and battery efficiency was observed, likely due to energy dissipation in side reactions that generate gas. Additionally, the setup could be improved, particularly the clips used for charging, which compress the coin cells and likely affect the external strain measurements.

Experiments conducted under both normal and abusive conditions demonstrated that rapid strain increases over small charge transfers can be an early indicator of battery malfunction, potentially preventing thermal runaway. The magnitude of strain measurements may indicate the defect state of the battery: higher strain suggests higher internal pressure and more gas formation, which could lead to thermal runaway. While temperature measurements were less dramatic, they supported these findings. This indicates that strain monitoring is a good method to provide early indication of battery malfunction, and is more reliable than temperature measurements.

Overall, FBGs exhibit the advantageous property of dual-parameter measurements, making them ideal for battery sensing. However, due to the intrinsic properties of coin cells, state estimation through FBG sensing proved difficult. Nevertheless, external FBG measurements on coin cells can serve as early indicators of battery malfunction, aiding in the detection of battery degradation and potentially preventing thermal runaway.

---

## 6 Further Work

This thesis discusses the use of FBG measurements to estimate the state and health of batteries, as well as the limitations of the experimental setup used in this study. The intrinsic properties of coin cells limit battery state estimation, as observed through the lack of correlation in the data. Embedding the fibers in the coin cell could be a solution to improve the sensing of temperature and strain during normal operating conditions. However, this is a more complex procedure, and the literature suggests that there are problems with the sealing of the cell. A soft casing, such as that of pouch cells, could also improve strain sensing because the flexible casing is more responsive to volume changes. Additionally, the small size and low capacity of the coin cell result in overall less heat and gas generation during normal cycling and under abusive conditions compared to higher-capacity batteries.

Further, investigating different types of battery materials may also provide a comparative analysis of how these factors influence strain and temperature readings. In addition, utilizing high-precision strain FBGs, such as those used by Peng et al., could provide higher sensitivity, and consequently better estimation of the SoC, SoH, and early detection of battery malfunctioning.

Expanding the range of operating conditions, such as varying the charge/discharge rates and ambient temperatures, would help to understand the robustness of FBG measurements under different scenarios. Additionally, some of the cycling schedules were aborted due to safety mechanisms in the Arbin system. Cycling the batteries with FBGs beyond this stage would provide more comprehensive data on the stages leading up to thermal runaway. This could reveal information on the evolution of reactions through the different stages and up until the cell catches fire. Implementing real-time data analysis and machine learning techniques could also improve the prediction accuracy of battery health and safety indicators based on FBG data.

To accurately understand and correlate the events occurring inside the battery during formation cycling with what is seen during later cycling, techniques such as cyclic voltammetry or X-ray diffraction could have been employed. These tests would be beneficial for understanding the processes, reactions, and phase transitions that occur during early cycling and relating them to the observed strain and temperature increases in the battery.

The coin cells were cycled using clips that compressed the external casing, which likely affected the results. Consequently, it would be beneficial to use a more gentle charging setup for future experiments to minimize external strain influences. Additionally, the absence of a fixed setup for the coin cells and FBGs introduced variability in the measurements. To address this, developing a 3D-printed box or a similar fixture could standardize the positioning of the FBGs. Further, it could be beneficial to restrain the surrounding environment more than was done in this research. Consequently, it may be beneficial to have the coin cells with FBGs within a thermally sealed box. This would ensure that the FBGs are consistently fixed at the same point on each cell while minimizing the environmental effects, thereby improving the accuracy and repeatability of the measurements.

## References

- [1] F. Mohammadi and M. Saif. “A comprehensive overview of electric vehicle batteries market”. In: *Advances in Electrical Engineering, Electronics and Energy* 3 (2023), p. 100127. URL: <https://www.sciencedirect.com/science/article/pii/S2772671123000220> (visited on 05/03/2024).
- [2] J. Peng *et al.* “State estimation of lithium-ion batteries based on strain parameter monitored by fiber Bragg grating sensors”. In: *Journal of Energy Storage* 52, Part B (2022), p. 104950. URL: <https://www.sciencedirect.com/science/article/pii/S2352152X22009562> (visited on 02/16/2024).
- [3] United Nations. *Li-ion batteries – powering the fossil-fuel-free economy*. URL: <https://www.un.org/en/Frontier-Technologies-Issues> (visited on 05/03/2024).
- [4] S. T. Boles *et al.* “Sensing as the key to battery lifetime and sustainability”. In: *Nature Sustainability* 5 (2022), pp. 194–204. URL: <https://www.nature.com/articles/s41893-022-00859-y> (visited on 09/18/2023).
- [5] Y. Chen *et al.* “A review of lithium-ion battery safety concerns: The issues, strategies, and testing standards”. In: *Journal of Energy Chemistry* 59 (2021), pp. 83–99. URL: <https://www.sciencedirect.com/science/article/pii/S2095495620307075> (visited on 06/01/2024).
- [6] Y. Rao. “In-fibre Bragg grating sensors”. In: *Measurement Science and Technology* 8 (1997), p. 355. URL: <https://iopscience.iop.org/article/10.1088/0957-0233/8/4/002> (visited on 04/17/2024).
- [7] S. J. An *et al.* “The state of understanding of the lithium-ion-battery graphite solid electrolyte interphase (SEI) and its relationship to formation cycling”. In: *Carbon* 105 (2016), pp. 52–76. URL: <https://www.sciencedirect.com/science/article/pii/S0008622316302676> (visited on 05/06/2024).
- [8] N.E. Galushkin *et al.* “Mechanism of Gases Generation during Lithium Ion Batteries Cycling”. In: *Journal of The Electrochemical Society* 166 (2019), A897. URL: <https://iopscience.iop.org/article/10.1149/2.0041906jes/pdf> (visited on 10/10/2023).
- [9] M. Daigle and C. S. Kulkarni. “Electrochemistry-based Battery Modeling for Prognostics”. In: *Annual Conference of the PHM Society* 5 (2013), p. 2252. URL: <https://www.papers.phmsociety.org/index.php/phmconf/article/view/2252> (visited on 09/23/2023).
- [10] J. Meyer *et al.* “Fiber optical sensors for enhanced battery safety”. In: *Fiber Optic Sensors and Applications XII*. Vol. 9480. 2015, pp. 190–201. URL: <https://www.spiedigitallibrary.org/conference-proceedings-of-spie/9480/94800Z/Fiber-optical-sensors-for-enhanced-battery-safety/10.1117/12.2183325.full> (visited on 05/27/2024).
- [11] X. Yang *et al.* “Modeling of lithium plating induced aging of lithium-ion batteries: Transition from linear to nonlinear aging”. In: *Journal of Power Sources* 360 (2017), pp. 28–40. URL: <https://www.sciencedirect.com/science/article/pii/S0378775317307619> (visited on 05/24/2024).



- 
- [12] Y. Cui et al. “Thermal Runaway Early Warning and Risk Estimation Based on Gas Production Characteristics of Different Types of Lithium-Ion Batteries”. In: *Batteries* 9 (2023), p. 438. URL: <https://www.mdpi.com/2313-0105/9/9/438> (visited on 05/27/2024).
- [13] G. Yang et al. “Real-time temperature measurement with fiber Bragg sensors in lithium batteries for safety usage”. In: *Measurement* 46 (2013), pp. 3166–3172. URL: <https://www.sciencedirect.com/science/article/pii/S0263224113002194> (visited on 02/12/2024).
- [14] A. Fortier et al. “Preliminary Study on Integration of Fiber Optic Bragg Grating Sensors in Li-Ion Batteries and In Situ Strain and Temperature Monitoring of Battery Cells”. In: *Energies* 10 (2017), p. 838. URL: <https://www.mdpi.com/1996-1073/10/7/838> (visited on 06/01/2024).
- [15] Y. Qiu and F. Jiang. “A review on passive and active strategies of enhancing the safety of lithium-ion batteries”. In: *International Journal of Heat and Mass Transfer* 184 (2022), p. 122288. URL: <https://www.sciencedirect.com/science/article/pii/S0017931021013879> (visited on 05/21/2024).
- [16] H. Shi et al. “Graphite structure and lithium intercalation”. In: *Journal of Power Sources* 68 (1997), pp. 291–295. URL: <https://www.sciencedirect.com/science/article/pii/S0378775396025621> (visited on 05/12/2024).
- [17] V. A. Sethuraman et al. “Surface structural disordering in graphite upon lithium intercalation/deintercalation”. In: *Journal of Power Sources* 195 (2010), pp. 3655–3660. URL: [https://www.sciencedirect.com/science/article/pii/S0378775309022964?ref=pdf\\_download&fr=RR-2&rr=883038d15a57712b](https://www.sciencedirect.com/science/article/pii/S0378775309022964?ref=pdf_download&fr=RR-2&rr=883038d15a57712b) (visited on 05/13/2024).
- [18] J. N. Reimers and J. R. Dahn. “Electrochemical and In Situ X-Ray Diffraction Studies of Lithium Intercalation in  $\text{LiCoO}_2$ ”. In: *Journal of The Electrochemical Society* 139 (1992), p. 2091. URL: <https://iopscience.iop.org/article/10.1149/1.2221184/pdf> (visited on 05/23/2024).
- [19] M. Simolka. *Determination of Degradation Mechanisms During the Cyclic Ageing of Li-ion Batteries*. 2021. URL: [https://www.researchgate.net/publication/357810329\\_Determination\\_of\\_Degradation\\_Mechanisms\\_During\\_the\\_Cyclic\\_Ageing\\_of\\_Li-ion\\_Batteries](https://www.researchgate.net/publication/357810329_Determination_of_Degradation_Mechanisms_During_the_Cyclic_Ageing_of_Li-ion_Batteries) (visited on 05/13/2024).
- [20] C. Daniel and J. O. Besenhard. *Handbook of Battery Materials*. Vol. 2. Wiley-VCH, 2008.
- [21] F. Yang et al. “A study of the relationship between coulombic efficiency and capacity degradation of commercial lithium-ion batteries”. In: *Energy* 145 (2018), pp. 486–495. URL: <https://doi.org/10.1016/j.energy.2017.12.144> (visited on 11/22/2023).
- [22] A. J. Smith et al. “A High Precision Study of the Coulombic Efficiency of Li-Ion Batteries”. In: *Electrochemical and Solid-State Letters* 13 (2010), A177. URL: <https://iopscience.iop.org/article/10.1149/1.3487637/meta> (visited on 05/22/2024).
- [23] D. Lisbona and T. Snee. “A review of hazards associated with primary lithium and lithium-ion batteries”. In: *A review of hazards associated with primary lithium and*

- lithium-ion batteries* 89 (2011), pp. 434–442. URL: <https://linkinghub.elsevier.com/retrieve/pii/S095758201100067X> (visited on 12/01/2023).
- [24] A.Y. Mekonnen *et al.* *A Review of Cathode and Anode Materials for Lithium-Ion Batteries*. 2016. URL: [https://www.researchgate.net/publication/306063848\\_A\\_review\\_of\\_cathode\\_and\\_anode\\_materials\\_for\\_lithium-ion\\_batteries](https://www.researchgate.net/publication/306063848_A_review_of_cathode_and_anode_materials_for_lithium-ion_batteries) (visited on 09/26/2023).
- [25] A. Eftekhari. “On the Theoretical Capacity/Energy of Lithium Batteries and Their Counterparts”. In: *ACS Sustainable Chem. Eng.* 7 (2018), pp. 3684–3687. URL: <https://doi.org/10.1021/acssuschemeng.7b04330> (visited on 12/15/2023).
- [26] M. N. Obrovac and V. L. Chevrier. “Alloy Negative Electrodes for Li-Ion Batteries”. In: 23 (2014). URL: <https://doi.org/10.1021/cr500207g> (visited on 05/07/2024).
- [27] Y. Zhang *et al.* “In Operando Monitoring the Stress Evolution of Silicon Anode Electrodes during Battery Operation via Optical Fiber Sensors”. In: *Small* (2024), p. 11299. URL: <https://onlinelibrary.wiley.com/doi/abs/10.1002/sml1.202311299> (visited on 03/01/2024).
- [28] N. Mohamed and N. K. Allam. “Recent advances in the design of cathode materials for Li-ion batteries”. In: *RSC Advances* 10 (2020), pp. 21662–21685. URL: <https://pubs.rsc.org/en/content/articlepdf/2020/ra/d0ra03314f> (visited on 06/01/2024).
- [29] C. M. Julien *et al.* “Comparative Issues of Cathode Materials for Li-Ion Batteries”. In: *Inorganics* 2 (2014), pp. 132–154. URL: <https://www.mdpi.com/2304-6740/2/1/132> (visited on 12/15/2023).
- [30] J. Banerjee and K. Dutta. “Materials for Electrodes of Li-Ion Batteries: Issues Related to Stress Development”. In: *Critical Reviews in Solid State and Materials Sciences* 42 (2016), pp. 218–238. URL: <https://www.tandfonline.com/doi/full/10.1080/10408436.2016.1173011> (visited on 10/05/2023).
- [31] L. Zhang *et al.* “High-safety separators for lithium-ion batteries and sodium-ion batteries: advances and perspective”. In: *Energy Storage Materials* 41 (2021), pp. 522–545. URL: <https://doi.org/10.1016/j.ensm.2021.06.033> (visited on 10/09/2023).
- [32] P. Zhu *et al.* “A review of current collectors for lithium-ion batteries”. In: *Journal of Power Sources* 485 (2021), p. 229321. URL: <https://www.sciencedirect.com/science/article/pii/S0378775320316098> (visited on 05/14/2024).
- [33] J. Vetter *et al.* “Ageing mechanisms in lithium-ion batteries”. In: *Journal of Power Sources* 147 (2005), pp. 269–281. URL: <https://www.sciencedirect.com/science/article/pii/S0378775305000832?via%3Dihubs> (visited on 05/14/2024).
- [34] H. Xuebing *et al.* “A comparative study of commercial lithium ion battery cycle life in electrical vehicle: Aging mechanism identification”. In: *Journal of power sources* 251 (2014), pp. 38–54. URL: <https://www.sciencedirect.com/science/article/pii/S0378775313018569?via%3Dihub> (visited on 05/14/2024).
- [35] M. Murnane and A. Ghazel. *A Closer Look at State of Charge (SOC) and State of Health (SOH) Estimation Techniques for Batteries*. 2017. URL: <https://www.analog.com/media/en/technical-documentation/tech-articles/a-closer-look>

- k-at-state-of-charge-and-state-health-estimation-tech.pdf (visited on 09/18/2023).
- [36] B. Rente *et al.* “Lithium-Ion Battery State-of-Charge Estimator Based on FBG-Based Strain Sensor and Employing Machine Learning”. In: *IEEE Sensors Journal* 21 (2020), pp. 1453–1460. URL: <https://ieeexplore.ieee.org/stamp/stamp.jsp?tp=&arnumber=9165856> (visited on 02/15/2024).
- [37] Y. Qiu and F. Jiang. “A critical review of using the Peukert equation for determining the remaining capacity of lead-acid and lithium-ion batteries”. In: *Journal of power sources* 155 (2006), pp. 395–400. URL: <https://www.sciencedirect.com/science/article/pii/S0378775305007093> (visited on 05/21/2024).
- [38] S. N. Bryntesen *et al.* “Opportunities for the State-of-the-Art Production of LIB Electrodes—A Review”. In: *Energies* 14 (2021), p. 1406. URL: <https://www.mdpi.com/1996-1073/14/5/1406> (visited on 05/20/2024).
- [39] Y. Liu *et al.* “Current and future lithium-ion battery manufacturing”. In: *iScience* 24 (2021), p. 102332. URL: <https://www.ncbi.nlm.nih.gov/pmc/articles/PMC8050716/> (visited on 09/28/2023).
- [40] D. L. Wood *et al.* “Formation Challenges of Lithium-Ion Battery Manufacturing”. In: *Joule* 3 (2019), pp. 2884–2888. URL: [https://www.cell.com/joule/pdf/S2542-4351\(19\)30532-X.pdf](https://www.cell.com/joule/pdf/S2542-4351(19)30532-X.pdf) (visited on 03/18/2024).
- [41] C. Mao *et al.* “Balancing formation time and electrochemical performance of high energy lithium-ion batteries”. In: *Journal of Power Sources* 402 (2018), pp. 107–115. URL: <https://www.sciencedirect.com/science/article/abs/pii/S037877531830990X> (visited on 12/14/2023).
- [42] J. Asenbauer *et al.* “The success story of graphite as a lithium-ion anode material – fundamentals, remaining challenges, and recent developments including silicon (oxide) composites”. In: *Sustainable Energy Fuels* 4 (2020), pp. 5387–5416. URL: <https://pubs.rsc.org/en/content/articlehtml/2020/se/d0se00175a> (visited on 05/27/2024).
- [43] D. H. Jeon. “Wettability in electrodes and its impact on the performance of lithium-ion batteries”. In: *Energy Storage Materials* 18 (2019), pp. 139–147. URL: <https://www.sciencedirect.com/science/article/pii/S2405829718312820> (visited on 03/05/2024).
- [44] S. K. Mohammadian *et al.* “Improving wettability and preventing Li-ion batteries from thermal runaway using microchannels”. In: *International Journal of Heat and Mass Transfer* 118 (2017), pp. 911–918. URL: <https://www.sciencedirect.com/science/article/pii/S001793101733380X> (visited on 03/18/2024).
- [45] S. J. An *et al.* “Fast formation cycling for lithium ion batteries”. In: *Journal of Power Sources* 342 (2017). URL: <https://www.sciencedirect.com/science/article/pii/S0378775317300113> (visited on 03/18/2024).
- [46] T. S. Pathan *et al.* “Active Formation of Li-Ion Batteries and Its Effect on Cycle Life”. In: *Journal of Physics: Energy* 1 (2019), p. 044003. URL: <https://iopscience.iop.org/article/10.1088/2515-7655/ab2e92> (visited on 12/11/2023).

- 
- [47] ACEY. *The role of the Glove Box in the Lithium-ion Battery Industry*. 2021. URL: [https://www.xmacey.com/the-role-of-the-glove-box-in-the-lithium-ion-battery-industry\\_n51](https://www.xmacey.com/the-role-of-the-glove-box-in-the-lithium-ion-battery-industry_n51) (visited on 02/21/2024).
- [48] L. Zheng *et al.* “Effects of Water Contamination on the Electrical Properties of 18650 Lithium Ion Batteries”. In: *Russian Journal of Electrochemistry* 50 (2013), pp. 904–907. URL: <https://link.springer.com/article/10.1134/S1023193514090122> (visited on 02/20/2024).
- [49] U. Heider *et al.* “Challenge in manufacturing electrolyte solutions for lithium and lithium ion batteries quality control and minimizing contamination level”. In: *Journal of Power Sources* 81-82 (2021), pp. 119–122. URL: <https://www.sciencedirect.com/science/article/pii/S0378775399001421> (visited on 02/21/2024).
- [50] A. Barré *et al.* “A review on lithium-ion battery ageing mechanisms and estimations for automotive applications”. In: *Journal of Power Sources* 241 (2013), pp. 680–689. URL: <https://www.sciencedirect.com/science/article/pii/S0378775313008185> (visited on 05/14/2024).
- [51] K. T. Lee *et al.* “Roles of Surface Chemistry on Safety and Electrochemistry in Lithium Ion Batteries”. In: *Accounts of Chemical Research* 46 (2011), pp. 1161–1170. URL: <https://pubs.acs.org/doi/epdf/10.1021/ar200224h> (visited on 09/21/2023).
- [52] H. Tachikawa and A. Shimizu. “Diffusion Dynamics of the Li Atom on Amorphous Carbon: A Direct Molecular Orbital-Molecular Dynamics Study”. In: *The Journal of Physical Chemistry B* 110 (2006), pp. 20445–20450. URL: <https://pubs.acs.org/doi/epdf/10.1021/jp0616031> (visited on 05/13/2024).
- [53] R. J. Rice and R. L. McCreery. “Quantitative Relationship between Electron Transfer Rate and Surface Microstructure of Laser-Modified Graphite Electrodes”. In: *Anal. Chem.* 61 (1989), pp. 1637–1641. URL: <https://pubs.acs.org/doi/pdf/10.1021/ac00190a010> (visited on 05/13/2024).
- [54] N. Li *et al.* “Non-equilibrium insertion of lithium ions into graphite”. In: *Journal of Materials Chemistry* 9 (2021), p. 12080. URL: <https://pubs.rsc.org/en/content/articlepdf/2021/ta/d1ta02836g> (visited on 05/23/2024).
- [55] E. R. White *et al.* “Intercalation events visualized in single microcrystals of graphite”. In: *Nature Communications* 8 (2018), p. 1969. URL: <https://www.nature.com/articles/s41467-017-01787-8> (visited on 05/27/2024).
- [56] Z. Wang *et al.* “Overcharge-to-thermal-runaway behavior and safety assessment of commercial lithium-ion cells with different cathode materials: A comparison study”. In: *Journal of Energy Chemistry* 55 (2021), pp. 484–498. URL: <https://www.sciencedirect.com/science/article/pii/S2095495620305234> (visited on 04/10/2024).
- [57] R. A. Leising *et al.* “Abuse Testing of Lithium-Ion Batteries: Characterization of the Overcharge Reaction of LiCoO<sub>2</sub>/Graphite Cells”. In: *Journal of the Electrochemical Society* 148 (2001), A838–A844. URL: <https://www.scopus.com/record/display.uri?eid=2-s2.0-0000014535&origin=inward> (visited on 05/19/2024).

- [58] Y. Saito *et al.* “Thermal behaviors of lithium-ion cells during overcharge”. In: *Journal of Power sources* 97-98 (2001), pp. 693–696. URL: <https://www.sciencedirect.com/science/article/pii/S0378775301007030> (visited on 05/19/2024).
- [59] B. Rowden and N. Garcia-Araez. “A review of gas evolution in lithium ion batteries”. In: *Energy Reports* 6 (2020), pp. 10–18. URL: <https://doi.org/10.1016/j.egyrs.2020.02.022> (visited on 04/09/2024).
- [60] D. J. Xiong *et al.* “Interactions between Positive and Negative Electrodes in Li-Ion Cells Operated at High Temperature and High Voltage”. In: *Journal of The Electrochemical Society* 163 (2016), A546. URL: <https://iopscience.iop.org/article/10.1149/2.0951603jes> (visited on 04/09/2024).
- [61] L. D. Ellis *et al.* “Quantifying, Understanding and Evaluating the Effects of Gas Consumption in Lithium-Ion Cells”. In: *Journal of The Electrochemical Society* 164 (2017), A3518. URL: <https://iopscience.iop.org/article/10.1149/2.0191714jes> (visited on 04/09/2024).
- [62] Y. Su *et al.* “Fiber Optic Sensing Technologies for Battery Management Systems and Energy Storage Applications”. In: *Sensors* 21 (2021), p. 1397. URL: <https://www.mdpi.com/1424-8220/21/4/1397> (visited on 09/20/2023).
- [63] L. Spitthoff *et al.* “Online Internal Temperature Sensors in Lithium-Ion Batteries: State-of-the-Art and Future Trends”. In: *Frontiers in Chemical Engineering* 4 (), p. 804704. URL: <https://www.frontiersin.org/articles/10.3389/fceng.2022.804704>.
- [64] Z. Wei *et al.* “Future smart battery and management: Advanced sensing from external to embedded multi-dimensional measurement”. In: *Journal of Power Sources* 489 (2021), p. 229462. URL: <https://www.sciencedirect.com/science/article/pii/S0378775321000148> (visited on 05/22/2024).
- [65] L. H. J. Raijmakers *et al.* “A review on various temperature-indication methods for Li-ion batteries”. In: *Applied Energy* 240 (2019), pp. 918–945. URL: <https://www.sciencedirect.com/science/article/pii/S0306261919303757> (visited on 05/22/2024).
- [66] M. Duff and J. Towey. “Two Ways to Measure Temperature Using Thermocouples Feature Simplicity, Accuracy, and Flexibility”. In: *Analog Dialogue* 44 (2010), pp. 3–8. URL: <https://www.tayloredge.com/reference/Tables/thermocouple03.pdf> (visited on 05/22/2024).
- [67] T. Krause *et al.* “Methods for Quantifying Expansion in Lithium-Ion Battery Cells Resulting from Cycling: A Review”. In: *Energies* 17 (2024), p. 1566. URL: <https://www.mdpi.com/1996-1073/17/7/1566> (visited on 05/29/2024).
- [68] I. Escher *et al.* “A Practical Guide for Using Electrochemical Dilatometry as Operando Tool in Battery and Supercapacitor Research”. In: *Energy Technology* 10 (2022), p. 2101120. URL: <https://onlinelibrary.wiley.com/doi/abs/10.1002/ente.202101120> (visited on 05/29/2024).
- [69] B. Rieger *et al.* “Multi-directional laser scanning as innovative method to detect local cell damage during fast charging of lithium-ion cells”. In: *Journal of Energy Storage* 8 (2016), pp. 1–5. URL: <https://www.sciencedirect.com/science/article/pii/S2352152X16301384> (visited on 05/30/2024).

- 
- [70] T.G. Giallorenzi *et al.* “Optical Fiber Sensor Technology”. In: *IEEE Transactions on Microwave Theory and Techniques* 30 (1982), pp. 472–511. URL: [https://ieeexplore.ieee.org/abstract/document/1131089?casa\\_token=gViJlqyN9oAAAAA:Iv h7An--bSW07UMXESvSH3V6aVh3ufZA0wZ7R9QzngWGy401-0uKfc ofEJdDsOuVX-\\_jVA](https://ieeexplore.ieee.org/abstract/document/1131089?casa_token=gViJlqyN9oAAAAA:Iv h7An--bSW07UMXESvSH3V6aVh3ufZA0wZ7R9QzngWGy401-0uKfc ofEJdDsOuVX-_jVA) (visited on 12/06/2023).
- [71] G. Han *et al.* “A review on various optical fibre sensing methods for batteries”. In: *Renewable and Sustainable Energy Reviews* 150 (2021), p. 11514. URL: <https://www.sciencedirect.com/science/article/pii/S1364032121007930> (visited on 02/14/2024).
- [72] M. Nascimento *et al.* “Simultaneous Sensing of Temperature and Bi-Directional Strain in a Prismatic Li-Ion Battery”. In: *Batteries* 4 (2018), p. 23. URL: <https://www.mdpi.com/2313-0105/4/2/23> (visited on 12/04/2023).
- [73] M. S. Wahl *et al.* “The Importance of Optical Fibres for Internal Temperature Sensing in Lithium-ion Batteries during Operation”. In: *Energies* 14 (2021), p. 3617. URL: <https://www.mdpi.com/1996-1073/14/12/3617> (visited on 12/03/2023).
- [74] C. E. Campanella *et al.* “Fibre Bragg Grating Based Strain Sensors: Review of Technology and Applications”. In: *Sensors* 18 (2018), p. 3115. URL: <https://www.mdpi.com/1424-8220/18/9/3115> (visited on 12/04/2023).
- [75] A. Raghavan *et al.* “Monitoring the Strain Evolution of Lithium-Ion Battery Electrodes using an Optical Fiber Bragg Grating Sensor”. In: *Energy Technology* 4 (2016), pp. 851–855. URL: <https://onlinelibrary.wiley.com/doi/abs/10.1002/ente.201500514> (visited on 05/16/2024).
- [76] M. Nascimento *et al.* “Real time thermal monitoring of lithium batteries with fiber sensors and thermocouples: A comparative study”. In: *Measurement* 111 (2017), pp. 260–263. URL: <https://www.sciencedirect.com/science/article/pii/S026322411730489X> (visited on 12/04/2023).
- [77] F. Huang *et al.* “Real-Time Monitoring of Temperature Field Distribution of Three-Element LiB Lithium Battery Using FBG Arrays”. In: *IEEE Sensors Journal* 23 (2023), pp. 30473–30480. URL: <https://ieeexplore.ieee.org/abstract/document/10316231> (visited on 02/27/2024).
- [78] V. A. Sethuraman *et al.* “Real-time stress measurements in lithium-ion battery negative-electrodes”. In: *Journal of Power Sources* 206 (2012), pp. 334–342. URL: <https://www.sciencedirect.com/science/article/pii/S0378775312000730> (visited on 05/21/2024).
- [79] J. Peng *et al.* “High precision strain monitoring for lithium ion batteries based on fiber Bragg grating sensors”. In: *Journal of Power Sources* 433 (2019), p. 226692. URL: <https://www.sciencedirect.com/science/article/pii/S0378775319306639> (visited on 12/04/2023).
- [80] Y. Ee *et al.* “Lithium-Ion Battery State of Charge (SoC) Estimation with Non-Electrical parameter using Uniform Fiber Bragg Grating (FBG)”. In: *Journal of Energy Storage* 40 (2021), p. 102704. URL: <https://www.sciencedirect.com/science/article/pii/S2352152X21004394> (visited on 02/14/2024).
- [81] A. Raghavan *et al.* “Embedded fiber-optic sensing for accurate internal monitoring of cell state in advanced battery management systems part 1: Cell embedding method

- 
- and performance”. In: *Journal of Power Sources* 341 (2016), pp. 466–473. URL: <https://www.sciencedirect.com/science/article/pii/S0378775316316718> (visited on 02/15/2024).
- [82] K. M. Alcock. *The Thermal Monitoring and Management of Lithium-Ion Batteries*. 2023. URL: <https://napier-repository.worktribe.com/output/3406767> (visited on 02/20/2024).
- [83] M. Li *et al.* “Characterization of Temperature and Strain Changes in Lithium-Ion Batteries Based on a Hinged Differential Lever Sensitization Fiber Bragg Grating Strain–Temperature Simultaneous-Measurement Sensor”. In: *Sensors* 24 (2024), p. 412. URL: <https://www.mdpi.com/1424-8220/24/2/412> (visited on 02/19/2024).
- [84] M. S. A. Rani *et al.* “Investigation of biosourced carboxymethyl cellulose-ionic liquid polymer electrolytes for potential application in electrochemical devices”. In: *Ionics* 22 (2016), pp. 1855–1864. URL: <https://doi.org/10.1007/s11581-016-1728-8> (visited on 06/04/2024).
- [85] R. Tan *et al.* “High-precision calibration method for fiber Bragg grating strain sensing based on an optical lever”. In: *Optical Fiber Technology* 61 (2021), p. 102392. URL: <https://www.sciencedirect.com/science/article/pii/S1068520020303825> (visited on 02/27/2024).
- [86] Laerd Statistics. *Pearson Product-Moment Correlation - Statistical tutorials and software guides*. 2020. URL: <https://statistics.laerd.com/statistical-guides/pearson-correlation-coefficient-statistical-guide-2.php> (visited on 04/08/2024).

## A Fiber Bragg Grating Calibration

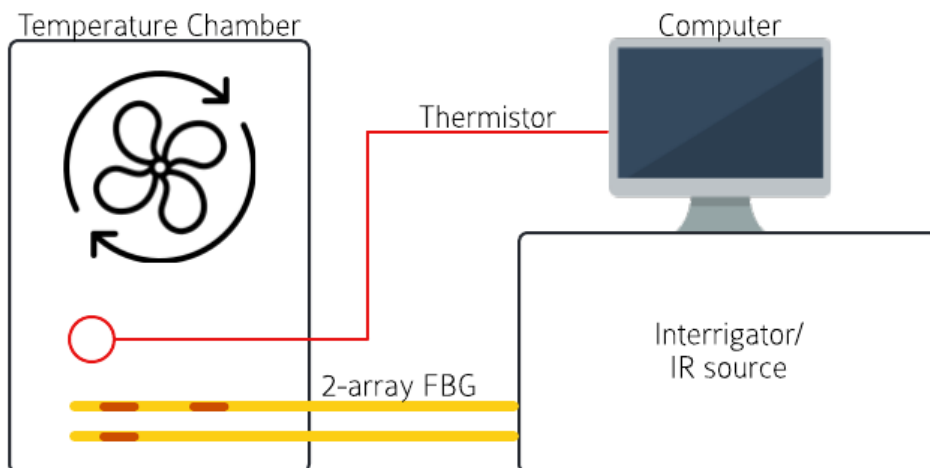


Figure A.1: Setup of the FBG calibration.

Figure A.1 illustrates the temperature calibration setup for the fiber Bragg grating sensors.

The calibration process and coin cell cycling took place within a temperature-controlled chamber (VWR INCU-Line, Cooled Incubators), where the FBG sensors and a thermistor were positioned in close proximity to minimize temperature discrepancies. The FBG sensors were connected to a HYPERION Optical Sensing Instrument, serving as both the infrared (IR) source and the spectrometer. The reflected data from the spectrometer is then sent to a computer where it is analyzed using ENLIGHT. The thermistor on the other hand was connected to Arbin’s computer program. Detailed specifics about the FBGs used are displayed in table A.1.

Table A.1: FBG specifications.

|                         | Reference Temperature<br>FBG | Temperature<br>FBG | Strain<br>FBG |
|-------------------------|------------------------------|--------------------|---------------|
| Central Wavelength [nm] | 1530.201                     | 1540.188           | 1540.209      |
| Bandwidth [nm]          | 0.223                        | 0.228              | 0.198         |
| SLSR [dB]               | 19.5                         | 24                 | 24            |
| Reflectivity            | 96.488%                      | 96.451%            | 96.321%       |
| Fiber Type              | Polyimide SMF-28e            |                    |               |
| Recoating               | Polyimed                     |                    |               |



## B Battery Capacity

The capacity of a LIB changes with different C-rates and the age of the battery. Although this topic extends beyond the primary focus of the thesis, it offers essential insights into why battery capacities diminish at higher C-rates. These findings help understand some of the practical implications discussed in the main body of the work.

Figure B.1 depicts a battery that is cycled at three different C-rates, 0.33C, 0.44C, and 0.55C, then back to 0.33C again.

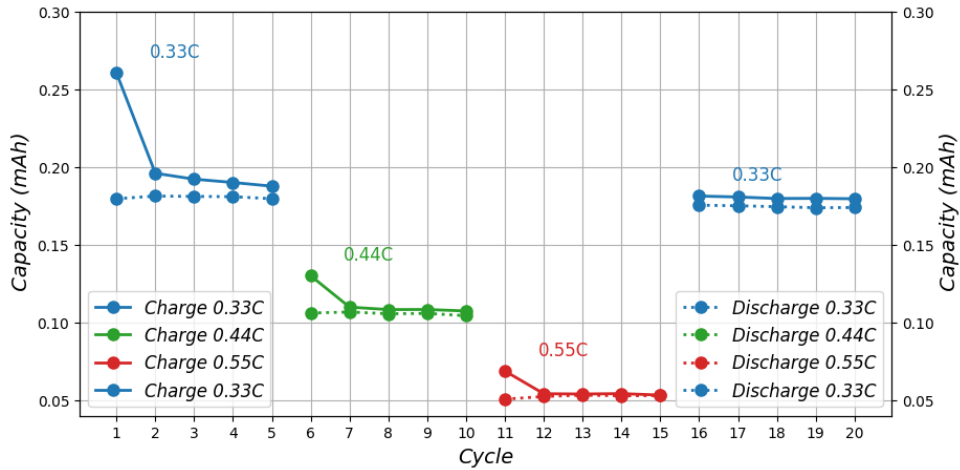


Figure B.1: Capacity for coin cell cycled at 0.33C, 0.44C and 0.55C, then back to 0.33C, for five cycles at each rate.

Observing the capacity at different C-rates (from 0.33C to 0.44C, then 0.55C and back to 0.33C), it is clear that the battery capacity tends to decrease as the C-rate increases. This is typical because higher C-rates can stress the battery more, leading to faster degradation or less efficient chemical reactions within the battery.

Further, the plot shows that when the C-rate is reduced back to 0.33C, the capacity does not fully recover to its initial values. This partial recovery can indicate some level of irreversible damage or change in the battery's chemistry or structure due to the higher C-rate cycles.



 **NTNU**

Norwegian University of  
Science and Technology